Fluid-driven transport of round sediment particles: from discrete simulations to continuum modeling (pre-print)

Qiong Zhang[1], Eric Deal[2], J. Taylor Perron[2], Jeremy G. Venditti[3], Santiago J. Benavides[2], Matthew Rushlow[2], Ken Kamrin[1]

[1]Department of Mechanical Engineering, Massachusetts Institute of Technology, Cambridge, Massachusetts, USA
[2]Department of Earth, Atmospheric, and Planetary Sciences, Massachusetts Institute of Technology, Cambridge, Massachusetts, USA
[3]Department of Geography, Simon Fraser University, Burnaby, British Columbia, Canada

Please note: This is a pre-print manuscript submitted to EarthArXiv. It has not undergone peer review. It has been submitted for publication, if accepted for publication the final version of the manscript will be made available.

Corresponding author: Ken Kamrin, kkamrin@mit.edu

Fluid-driven transport of round sediment particles: from discrete simulations to continuum modeling

Qiong Zhang[1], Eric Deal[2], J. Taylor Perron[2], Jeremy G. Venditti[3], Santiago J. Benavides[2], Matthew Rushlow[2], Ken Kamrin[1]

[1]Department of Mechanical Engineering, Massachusetts Institute of Technology, Cambridge, Massachusetts, USA
[2]Department of Earth, Atmospheric, and Planetary Sciences, Massachusetts Institute of Technology, Cambridge, Massachusetts, USA
[3]Department of Geography, Simon Fraser University, Burnaby, British Columbia, Canada

Key Points:

- Resolved particle-scale bedload transport simulations agree with flume experiments.
- Simulations probe the small-scale mechanisms and parameter dependences in the transport relation.
- Particle simulations guide continuum model development for turbulent sediment transport and bed creep.

Corresponding author: Ken Kamrin, `kkamrin@mit.edu`

Abstract

Bedload sediment transport is ubiquitous in shaping natural and engineered landscapes, but the variability in the relation between sediment flux and driving factors is not well understood. At a given Shields number, the observed dimensionless transport rate can vary over a range in controlled systems and up to several orders of magnitude in natural streams. Here we (1) experimentally validate a resolved fluid-grain numerical scheme (Lattice Boltzmann Method - Discrete Element Method or DEM-LBM), and use it to (2) explore the parameter space controlling sediment transport in simple systems. Wide wall-free simulations show the dimensionless transport rate is not influenced by the slope, fluid depth, mean particle size, particle surface friction, or grain-grain damping for gentle slopes (0.01 $\sim$ 0.03) at a medium to high fixed Shields number. (3) Examination of small-scale fluid-grain interactions shows fluid torque is non-negligible for the entrainment and sediment transport near the threshold. And (4) the simulations guide the formulation of continuum models for the transport process. We present an upscaled two-phase continuum model for grains in a turbulent fluid and validate it against bedload transport DEM-LBM simulations. To model the creeping granular flow under the bed surface, we use an extension of the Nonlocal Granular Fluidity (NGF) model, which was previously shown to account for flow cooperativity from grain-size-effects in dry media. The model accurately predicts the exponentially decaying velocity profile deeper into the bed.

Plain Language Summary

Sediment transport caused by particles rolling, sliding, and hopping on a river bed is called bedload transport. Semi-empirical formulas to predict bedload sediment flux from the driving factors, known as the transport relation, can be highly inaccurate. This paper uses simulations where the sediment particles are fully resolved to examine the particle parameters to find if the predictions can be improved by considering more parameters. After validating the numerical scheme against flume experiments, it is used to simulate bedload transport under many conditions, and its results show that at a fixed relative bed shear stress, varying river slope (on gentle slopes), fluid depth, mean particle size, particle surface sliding friction coefficient, and grain-grain damping coefficient cause almost no variation of the transport rate. We examine how the fluid torque on particles helps initiate rolling and subsequent grain transport. We further use the numerical scheme to guide development of a continuum framework that can predict the flow profiles in the rapid zone as well as the creep flow beneath the bed surface. The continuum approach is a more tractable way to model large-scale bedload sediment transport problems.

1 Bedload transport of spherical grains

Fluid-driven sediment transport, in which a flow passing over a loose granular bed entrains and moves the grains, plays a pivotal role in many natural and engineered landscapes. Common scenarios that require the calculation of sediment transport rates include conveyance of sediment through engineered channels, infilling of artificial reservoirs, dispersal of stored sediment following dam removal, and long-term sediment transport that shapes natural rivers (Gomez, 1991; Yalin & da Silva, 2001). Applications like these create a demand for sediment transport models that can be applied over a wide range of flow conditions and sediment characteristics.

However, calculation of sediment transport rates over a wide range of conditions is a challenging task. Sediment transport at the scale of a river channel depends on the fine-scale interaction of a turbulent flow with many individual sediment grains. Moreover, variations in these fluid-grain interactions through time, or with height above or below the sediment bed, can create different regimes of grain motion (Houssais et al.,

Table 1. Widely used bedload transport relations.

Author(s)	Dimensionless transport rate q^*	Critical Shields # τ_c^*
Meyer-Peter and Müller (1948)	$q^* = 8(\tau^* - \tau_c^*)^{3/2}$	$\tau_c^* = 0.047$
Ashida and Michiue (1973)	$q^* = 17(\tau^* - \tau_c^*)(\sqrt{\tau^*} - \sqrt{\tau_c^*})$	$\tau_c^* = 0.05$
Engelund and Fredsøe (1976)	$q^* = 18.74(\tau^* - \tau_c^*)(\sqrt{\tau^*} - 0.7\sqrt{\tau_c^*})$	$\tau_c^* = 0.05$
Fernandez-Luque and Van Beek (1976)	$q^* = 5.7(\tau^* - \tau_c^*)^{3/2}$	$\tau_c^* = 0.037 \sim 0.0455$
Wong (2003)	$q^* = 3.97(\tau^* - \tau_c^*)^{3/2}$	$\tau_c^* = 0.0495$

2015), including creep of closely packed grains, a rapidly shearing slurry, or a dilute suspension.

Bedload sediment flux, in which grains move by rolling, sliding or hopping along the bed, is practically described by field-scale sediment transport models which are typically derived semi-empirically by comparing the bulk characteristics of flows, such as average bed shear stress, with observations of bulk sediment transport rates from laboratory flume experiments (Meyer-Peter & Müller, 1948; Ashida & Michiue, 1973; Fernandez-Luque & Van Beek, 1976; Wiberg & Smith, 1989; Wong, 2003). Less commonly, field monitoring studies are used (Bagnold, 1980; Gomez, 1991). Some widely used bedload transport relations are listed in Table 1, where the dimensionless sediment transport rate (the Einstein number) is

$$q^* \equiv q_s \Big/ \left(d_p \sqrt{\frac{\rho_s - \rho_f}{\rho_f} g d_p} \right), \tag{1}$$

with q_s the sediment volume flux per unit flow width, d_p the grain diameter, and ρ_s and ρ_f the sediment and fluid densities. The dimensionless bed shear stress, often referred to as the Shields number, is

$$\tau^* \equiv \tau_b \big/ \left[(\rho_s - \rho_f)\, g d_p \right], \tag{2}$$

with τ_b the bed shear stress and g the gravitational acceleration. Most bedload transport relations have a critical value of the Shields number τ_c^* at which grains begin to move (Shields, 1936), and most converge to a power law of 3/2 for $\tau^* \gg \tau_c^*$, but differ if τ^* is close to the threshold of grain motion (Lajeunesse et al., 2010). Recently, Pähtz and Durán (2020) proposed a formula in which $q*$ scales with $\tau^* - \tau_c^*$ linearly for $\tau^* \to \tau_c^*$ and quadratically for $\tau^* \gg \tau_c^*$ through numerical simulations, indicating the 3/2 power law may be an approximation between these two ends.

These semi-empirical models have the desirable characteristic that they are easy to apply in natural and experimental settings, and they are therefore widely used. However, even under controlled laboratory conditions, empirical bedload transport expressions commonly over- or under-predict sediment flux by more than a factor of two (Lajeunesse et al., 2010); and larger disagreements in natural settings are common: Reid and Laronne (1995) compiled the data from 6 streams and found that q^* can vary by a factor of 10 across tests with τ^* fixed at $\tau^* = 0.02$ and more than 100 (up to 1000) when $\tau^* \sim 0.1$. Correction factors for q^*, τ^* and τ_c^* for steep slopes can be obtained from recent works (Maurin et al., 2018; Pähtz & Durán, 2020) . However, the variability is evident even in sediment transport experiments on gentle slopes, such as Meyer-Peter and Müller (1948) in which the slope $S < 0.02$and the above slope correction factors are close to 1. What is causing the variation in flux (q^*) for a given Shields number (τ^*) on gentle slopes? The empirical transport expressions are also remarkable for what they do not contain, such as any dependence on sediment geometric or surface characteristics other than a representative grain diameter. There are reasons to expect that grain-scale phenomena influence channel-scale sediment transport, but which grain-scale phenomena do we need to consider?

One way to address this question is to simulate the grain-scale mechanisms that entrain and transport sediment. Recent computational and methodological advances have made it feasible to numerically investigate the mutual interactions of many sediment grains and a turbulent flow, allowing for interrogation of transport phenomena at a level of detail that is difficult to achieve even in well-instrumented experiments. Simulations in which the sediment particles are treated as discrete elements can be classified into two types based on the way the fluid-particle interaction is handled: (1) the fluid grid size is much smaller than the particle size so that the fluid-particle interaction can be resolved (Derksen, 2015). And (2) the fluid grid size is comparable to or larger than the particle size and the fluid-particle interaction is modeled by a drag (hydrodynamic force) law (Schmeeckle, 2014, 2015), and potentially also a hydrodynamic torque model (Finn et al., 2016; Guan et al., 2021). Most of the simulations examining the sensitivity of the transport relation to the microscopic particle parameters adopt the second type for the higher computational efficiency; e.g. recent studies (Maurin et al., 2015; Elghannay & Tafti, 2018; Pähtz & Durán, 2018b, 2018a) have found that the transport relation is insensitive to the particle surface friction coefficient and the restitution coefficient. But these simulations do not include the hydrodynamic torque on particles, which may be important since rolling has lower threshold than sliding in entrainment events (Dey & Ali, 2017). The lack of fluid-particle angular momentum exchange may cause problems in the other direction as well: the rotation of a single sediment particle near the bed surface influences the fluid vortex structure nearby which in return changes the hydrodynamic forces (C. Zhang et al., 2017). Also, for grains near the bed surface where we would want the most accuracy, the separation of length scales presumed in a drag model might not be applicable due to the jump in volume fraction, which could render the drag model less accurate. These questions matter most for sediment transport close to τ_c^*. Laminar transport simulations (Derksen, 2011), which resolve the fluid-particle linear and angular momentum exchange, have shown that the rolling mode in the incipient motion requires nonzero surface friction coefficient, but the specific value of the friction coefficient has only marginal influence. But its effect is still not known in turbulent sediment transport. These considerations motivate revisiting the parameter space, especially the microscopic particle parameters (such as the friction coefficient and the restitution coefficient), using turbulent sediment transport simulations which resolve the fluid-particle interaction at a sub-grain scale.

However, even if grain-resolving simulations give us all the answers, they are currently impractical to implement at field scale (i.e. the scale of a river channel). So one option, as a complementary approach, would be to use them to help parameterize/validate a continuum model that could be scaled up more easily and captures the rheological behavior of grains and fluid in different regions of the bed and the flow. As noted previously, a given fluid stress can cause grains at different heights below or above the sediment bed to move in different granular flow regimes, ranging from a thick creeping layer to a dense slurry to a dilute suspension. Houssais et al. (2015) analyze the threshold of grain motion from this perspective, and show in a set of laboratory experiments that the transition from no motion to bedload transport as τ^* increases is a gradual transition (as opposed the discontinuous transition implicitly assumed by equations in Table 1) characterized by progressive quickening of granular creep throughout a layer that extends many grain diameters below the bed surface. They additionally propose a regime diagram for sediment transport in which the style of grain motion (creep, bedload, or dilute) depends on the height relative to the bed surface and the transport stage, τ^*/τ_c^*. This alternate perspective on sediment transport implies that it may be possible to improve predictions of sediment flux by describing these granular regimes with appropriately coupled rheological models rather than fitting a single function to experimental data over a range of $\tau^* - \tau_c^*$.

In this paper, in order to understand the variability of sediment flux (q^*) at a given Shields number (τ^*), we examine three questions: (i) How important is fluid-particle angular momentum transfer and in which part of the flow and in which regime of the sediment transport is it important? We fully resolve the grain-scale spherical particle movement and study the fluid-particle angular momentum exchange studied in an entrainment event. Then it is quantified as a "rotation stress" whose profile is examined in different transport stages and further correlated to the transport relation. Our work here is benchmarked by flume experiments (Deal et al., 2021; Benavides et al., 2021) in which grain-scale motions were tracked. (ii) What is (not) responsible for the variability in the observed sediment transport relation? We explore the parameter space (macroscopic river settings such as slope, and most importantly microscopic particle parameters such as the mean size, surface roughness, and grain contact damping) to see what is responsible for the variability in the relation between the Einstein number and the Shields number in turbulent sediment transport. (iii) How can we formulate a useful model broadly applicable at different scales across the range of bedload sediment transport behaviors? We use the DEM-LBM simulation data to derive continuum models of sediment transport that apply to a range of flow conditions and sediment characteristics. For simplicity, we will limit our investigation to the bedload sediment transport of mono-disperse particles without considering vegetation (Vargas-Luna et al., 2015; C. Liu et al., 2021), external agitation of the turbulence (Sumer et al., 2003; Ojha et al., 2019; Cheng et al., 2020), or channel morphology that is known to influence the transport relation, such as bedform patterns (Venditti, 2013; Venditti et al., 2017) or the presence of large (possibly not fully submerged) boulders (Yager et al., 2007).

2 Discrete simulations

A few geoscience-oriented studies have begun to probe the physics of grain-scale sediment motion through numerical experiments (Schmeeckle & Nelson, 2003; Schmeeckle, 2014, 2015; Hill & Tan, 2017). Schmeeckle (2014) pioneered this approach in geomorphology by coupling discrete element method (DEM) simulations of grain motion with large-eddy simulations (LES) of turbulent flow. He found that coherent flow structures impinging on the bed are a major cause of sediment entrainment, and he measured a power-law relationship between q^* and τ^* that is similar to (but somewhat steeper than) the widely used bedload transport expression (Wong & Parker, 2006; Meyer-Peter & Müller, 1948). The LES-DEM approach employed by Schmeeckle (2014), a variant of the general CFD-DEM method (CFD: computational fluid dynamics) for the fluid and particles, does not explicitly model flow around grains or particle-scale pressure variations (e.g. lubrication forces). Instead, the flow and grains are coupled with spatially averaged body forces. Nonetheless, his promising results suggest that direct simulations of sediment transport with tighter fluid-grain coupling will yield even more insight into the controls on bedload flux. In recent years, more researchers have studied sediment transport problems using similar CFD-DEM simulations. For example, Hill and Tan (2017) studied the influence of the added fine particles on the mobilization of gravel beds using LES-DEM. Maurin et al. (2018) and Pähtz and Durán (2020) studied slope influence in sediment transport and have proposed slope corrections for q^*, τ^* and τ_c^* for steep slopes. Finn et al. (2016) simulated particle dynamics on wavy bottoms. Most recently, Guan et al. (2021) studied Kelvin–Helmholtz vortices' influence on local and instantaneous bedload sediment transport with the same numerical method as Finn et al. (2016).

For sub-particle resolution of the fluid-grain interaction, the Lattice Boltzmann Method (LBM) (H. Chen et al., 1992) is able to resolve the fluid-particle interaction at the moving particle boundaries (Boutt et al., 2007; Derksen, 2015; Amarsid et al., 2017) by treating the fluid material as hypothetical fluid particles marching in space and colliding with

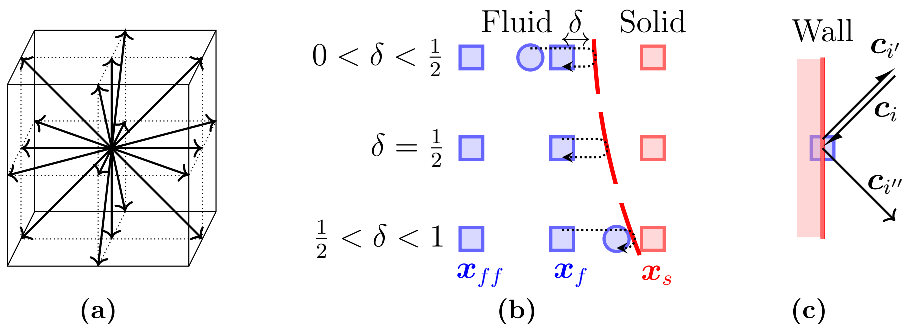

Figure 1. Lattice Boltzmann Method: (a) The velocity set of D3Q19: 18 velocities streaming out from the node to the next nearest nodes in the velocity directions and a rest velocity staying at the original node (b) Particle boundary treatment in LBM, depending on δ the distance from the last fluid node to the boundary in terms of lattice units. $\boldsymbol{x}_f$ is the fluid node next to a solid node $\boldsymbol{x}_s$, and $\boldsymbol{x}_{ff}$ is the neighbor fluid node upstream. (c) Related velocities near a stationary wall (the fluid node is aligned with the wall): the fluid parcel coming in $\boldsymbol{c}_i$ will be bounced back into the opposite direction $\boldsymbol{c}_{i'}$ at a no-slip wall, and will be reflected specularly into $\boldsymbol{c}_{i''}$ at a free-slip wall.

the solid particle boundaries. Coupled DEM-LBM simulations can fully resolve the fluid-particle interaction in sediment transport problems and offer more understanding about the grain-scale mechanisms.

In the following discussion of the particle-scale simulations, we first introduce the DEM-LBM numerical method. Second, we present simulations matching the conditions of flume experiments (Deal et al., 2021; Benavides et al., 2021) to provide a relevant many-particle test of the methodology. Third, we present wide wall-free simulations in order to study the factors that can potentially cause the variability seen in experimental transport data on gentle slopes.

2.1 Method: DEM-LBM

The translation and rotation of the sediment particles in our DEM-LBM simulations are integrated from the equations of motion of individual particles using the Velocity Verlet method (Swope et al., 1982), which is widely used in DEM simulations of granular materials and is implemented in common software such as LAMMPS (Plimpton, 1995) and LIGGGHTS (Kloss et al., 2012). The particle-particle interaction is elastic with damping effects in the normal direction, which can be simulated as a spring-dashpot model, and the interaction is elastic with friction in the tangential direction.

The DEM algorithm is fully coupled to a LBM solver, which can resolve the traction over many moving boundaries (grain surfaces in our case). S. Chen and Doolen (1998) review the history of this numerical method, and Aidun and Clausen (2010) review the application of LBM to complex flows. Inspired by the Boltzmann-Maxwell Equation, LBM recovers the Navier-Stokes equations (H. Chen et al., 1992) by treating the fluid material as hypothetical fluid packets that collide and stream in a discrete set of directions. The method is particularly advantageous for solving problems with many moving boundaries and the simple form makes implementation straightforward.

In a standard LBM algorithm, the domain is discretized into a uniform orthogonal grid. The fluid material exists in the 3D domain only on the nodes in a certain discretized dimensionless velocity set $\{\boldsymbol{c}_i\}$. In this work, we choose a discretization composed of of 19 directions, known as D3Q19, as shown in Figure 1(a). The fluid material at a point is represented by “fluid parcels” streaming in 18 directions with magnitudes that move the parcels to the nearest node in the velocity direction through each LBM timestep (with the 19th parcel just resting at the original node). Each of the parcels corresponds to a distribution function component f_i satisfying $\Sigma_{i=0}^{18} f_i = 1$. In a fluid timestep, as shown in Eq 3, the fluid undergoes a collision (right-hand side) and a streaming operation (left-hand side) sequentially:

$$\underbrace{f_i(\boldsymbol{x}+\boldsymbol{c}_i, t+1) - f_i(\boldsymbol{x}, t)}_{\text{Streaming}} = \underbrace{\frac{1}{\tau}\left[f_i^{eq} - f_i\right]}_{\text{Collision}}, \tag{3}$$

where $\boldsymbol{x}$ is the dimensionless position, τ is the dimensionless relaxation time and f_i^{eq} is the equilibrium distribution function. All the quantities are nondimensionalized by the grid size dx, LBM timestep dt_f, and ρ_f. In the collision operation, f_i^{eq} is a function of the macroscopic fluid velocity and density, and τ is a function of the local fluid kinematic viscosity ν (Yu et al., 2005):

$$\tau = \frac{1}{2} + \frac{3\nu}{dx^2/dt_f}. \tag{4}$$

For turbulent flow, a Large Eddy Simulation (LES) method (Yu et al., 2005) can model the subgrid-scale eddies. We use the Smagorinsky turbulent closure (Smagorinsky, 1963):

$$\nu = \nu_f + \nu_t, \quad \nu_t = (C_s \cdot dx)^2 \dot{\gamma}_f, \tag{5}$$

where ν_f is the kinematic viscosity of the pure fluid, ν_t is the turbulent viscosity, C_s Smagorinsky constant, and $\dot{\gamma}_f$ the fluid local shear rate. C_s is shown to be dependent on the discretization and geometry (Yoshizawa, 1993; Hou et al., 1994). We calibrate $C_s = 0.27$ in the flume geometry (see Appendix A for details and for validation of the pure fluid simulations) with grid size $dx = 0.5$mm. The value of C_s and the grid spacing are used throughout this paper for the simulations in which the fluid is water. Body forces such as gravity can be taken into account by adding an extra term to the collision step (Z. Guo et al., 2002). More details on how to construct a macroscopic variable such as $\dot{\gamma}_f$ from the distribution $\{f_i\}$ can be found in (Yu et al., 2005).

For a post-collision distribution function component f_i^c at the fluid node $\boldsymbol{x}_f$ next to a solid node $\boldsymbol{x}_s$, when the corresponding parcel hits a fixed solid boundary that sits in the middle of a link, it will bounce back and end up with the opposite direction $f_{i'}(\boldsymbol{x}_f, t+1) = f_i^c(\boldsymbol{x}_f, t)$, where $f_{i'}$ denotes the component in the opposite direction of f_i. As shown in Figure 1(b), when δ the distance from the last fluid node to the boundary is not exactly 0.5, the component $f_{i'}(\boldsymbol{x}_f, t+1)$ can be interpolated (Bouzidi et al., 2001). For $0 < \delta < \frac{1}{2}$, the interpolation happens before the streaming

$$\begin{aligned} f_{i'}(\boldsymbol{x}_f, t+1) &= f_i^c(\boldsymbol{x}_f + (2\delta - 1)\boldsymbol{c}_i, t) \\ &= 2\delta f_i^c(\boldsymbol{x}_f, t) + (1-2\delta) f_i^c(\boldsymbol{x}_{ff}, t), \end{aligned} \tag{6}$$

whereas for $\frac{1}{2} \le \delta \le 1$, interpolation happens after the streaming

$$\begin{aligned} f_{i'}(\boldsymbol{x}_f, t+1) &= \frac{1}{2\delta} f_{i'}(\boldsymbol{x}_f + (2\delta-1)\boldsymbol{c}_i, t+1) + \frac{2\delta - 1}{2\delta} f_{i'}(\boldsymbol{x}_{ff}, t+1) \\ &= \frac{1}{2\delta} f_i^c(\boldsymbol{x}_f, t) + \frac{2\delta-1}{2\delta} f_{i'}^c(\boldsymbol{x}_f, t), \end{aligned} \tag{7}$$

For moving solid boundaries, the no-slip boundary condition can be modified according to the velocity of the particle boundary due to translation and rotation (Bouzidi et al., 2001). In our flume simulations (Section 2.2), since the thickness of the boundary layer at the glass side walls is smaller than (or comparable to) the grid size dx, we developed a new boundary technique that accounts for the boundary layer implicitly through a matched slip boundary condition. See Appendix A for more details. At a free-slip boundary, the parcel will specularly reflect instead of bounce back (Ladd, 1994) as shown in Figure 1(c). As indicated above, all the LBM boundary conditions are processed in the streaming operation.

The local parcel momentum changes can be used to integrate the force and torque on individual particles exerted by the fluid (Mei et al., 2002). In this way, the fluid feels the moving particles through the moving interfaces, and the particles feel the fluid via the integrated hydrodynamic forces and torques. These will be used in the DEM scheme to update the linear and angular acceleration of the particles. Note that the timestep of the DEM dt to resolve the elastic interaction of particles (Da Cruz et al., 2005; Kamrin & Koval, 2012) is smaller than the timestep of the LBM $dt_f = dx/c_s$, where c_s is the fluid sound speed. dt_f is chosen so that the corresponding sound speed $c_s = dx/dt_f$ guarantees that the maximum Mach number is below 0.3, in the incompressible limit (Succi, 2001), and the distance a particle travels in a "free flight" is less than $0.02dx$ (mostly $< 0.01dx$) (Derksen, 2015). In the DEM-LBM simulations presented in this paper, a LBM step is called every 50 DEM steps to update the hydrodynamic forces and torque. If the DEM algorithm uses the particle-wise hydrodynamic forces (and torque) in the current LBM steps to update the particles' linear and angular acceleration, the interstitial fluid may experience numerical oscillations. As a remedy, the particle-wise hydrodynamic forces (and torque) in the current and the previous LBM steps are averaged when conducting the DEM update. When a particle is close to another particle or a wall, the algorithm searches for the upstream fluid information $f_i^c(\boldsymbol{x}_{ff}, t)$ or even $f_i^c(\boldsymbol{x}_f, t)$ in Eq 6 and Eq 7 which may be no longer physically available. Special care must be taken to update the fluid domain information as well as to calculate the corresponding fluid-solid momentum exchange. For these near contact scenarios, the needed upstream fluid distribution function component, $f_i^c(\boldsymbol{x}_{ff}, t)$ or $f_i^c(\boldsymbol{x}_f, t)$, is evaluated as the (Maxwell) equilibrium distribution using the grain velocity at the node if the search for the upstream fluid node goes into a node occupied by another particle. If the search goes out of the wall of the flume, then it comes back to the domain (see $\boldsymbol{c}_{i''}$ as shown in Figure 1(c)).

By refining the resolution of LBM with respect to the particle size d_p, Feng and Michaelides (2009) and Derksen (2014) have shown that a resolution of $dx \leq d_p/6$ or $dx \leq d_p/8$ is adequate for sufficiently accurate results. Here in this paper, $dx \leq\sim d_p/10$ is kept to guarantee enough accuracy. To run our method, we have extended a custom-written program described in Mutabaruka et al. (2014) and Mutabaruka and Kamrin (2018).

The DEM-LBM algorithm is validated at the grain scale in tests of the particle-fluid linear and angular momentum exchange as well as the resolved lubrication force between close moving solid boundaries. See Appendix B for more details.

2.2 Comparison with laboratory flume experiments

Deal et al. (2021) and Benavides et al. (2021) conducted bedload sediment transport experiments with glass spheres in a narrow flume, and recorded high-speed videos of the grains, allowing for precise tracking. This provides abundant details of the particle motion. We performed corresponding DEM-LBM simulations as validation specifically to test the accuracy of our method in sediment transport problems. We begin by comparing the time-averaged sediment transport rates as a first verification of our simulations, and then do a more detailed comparison of the time-averaged velocity profiles and particle velocity fluctuation profiles.

The schematic diagram of the flume experimental setup of Deal et al. (2021) and Benavides et al. (2021) is shown in Figure 2 (a). In each experiment, mono-disperse glass spheres and water are fed into the inclined flume from the upstream end at a given combination of volume flux rates. After the initial period of sphere deposition, the granular bed builds up and steady state is reached. Then the slope of the free water surface

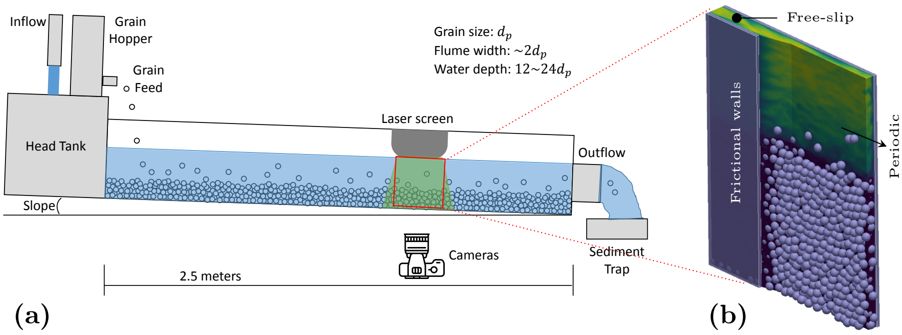

Figure 2. Setup of the sediment transport tests in the narrow flume. (a) Experimental setup (Deal et al., 2021; Benavides et al., 2021). (b) The simulated domain corresponds to the videoed zone in the experiment as shown in the red box.

S as well as the water depth are measured, and the particle motion is recorded by the high-speed cameras in the middle section of the flume. The flume is 10.2mm, slightly wider than two particle diameters ($d_p = 4.95$mm). The density of the spheres is $\rho_s = 2550\,\mathrm{kg/m^3}$. The elastic constants for the normal and tangential contacts are set to be $20\,000\,\mathrm{N\,m^{-1}}$ and $5714\,\mathrm{N\,m^{-1}}$, respectively, guaranteeing the spheres are in hard limit. The friction coefficients of sphere-sphere and sphere-sidewall contacts are measured to be 0.50 and 0.45 respectively. The dry restitution coefficient of the particles is 0.93. The sensitivity of the results to the choice of the particle surface parameters is low.

DEM-LBM simulations are set up with the same flume geometry and material properties. The simulated domain, as shown in 2 (b), has a length $L = 24d_p$ and height $30d_p$. When all the spheres are deposited (in total 969 particles), the thickness of the bed is $18d_p$. The thickness of the bed reduces to $15d_p$ for the largest Shields number tested, as some of the spheres are entrained by the fluid. The LBM lattice has homogeneous grid size $dx = 0.5$mm. The first and last nodes across the flume align with the side walls, and the simulated flume width is adjusted slightly to have $W = 10.5$mm. The top of the simulated domain uses a free-slip (zero gradient) boundary condition. Note that in this narrow flume configuration, the fluid velocity far above the granular bed surface approaches a constant value due to sidewall shear. The bottom uses a no-slip boundary condition and the two sides perpendicular to the flow direction use periodic boundary conditions. For the two side walls of the flume, since the thickness of the boundary layer is smaller than the grid size dx, no-slip boundary conditions with LES is not enough to resolve the near-wall flow field correctly. Instead, we developed a new boundary technique: assuming the second layer of nodes from the wall are out of the boundary layer, we extrapolate the law-of-the-wall flow relationship to the wall, and treat this value as a slip velocity at the wall, which we implement in DEM-LBM using Navier-type boundary conditions used in other studies (Uth et al., 2013; K. Wang et al., 2018, see Appendix A for more details). The gravity $g = 9.8\,\mathrm{m/s^2}$ is applied at an angle of slope S with respect to the vertical axis of the simulated domain. The flow is driven by the tilted "horizontal" gravity component.

For the calculation of τ^*, the bed shear stress τ_b is calculated as $\tau_b = \rho_f g S \frac{HW}{2H+W}$, where H is the water depth measured down to the bed surface and W is the flume width. Mindful of the lengthy compute times for each simulation, we chose to perform simulations at 5 different slopes, corresponding to $\tau^* = 0.023$, 0.028, 0.047, 0.063 and 0.068, which covers the experimental range. For the calculation of q^*, the sediment volume flux per unit width q_s is counted in the whole domain as $q_s = \Sigma_i \frac{\pi}{6} d_p^3 V_{i,x}/LW$, where $V_{i,x}$ is the streamwise velocity of the i-th particle and L is the length of the simulated do-

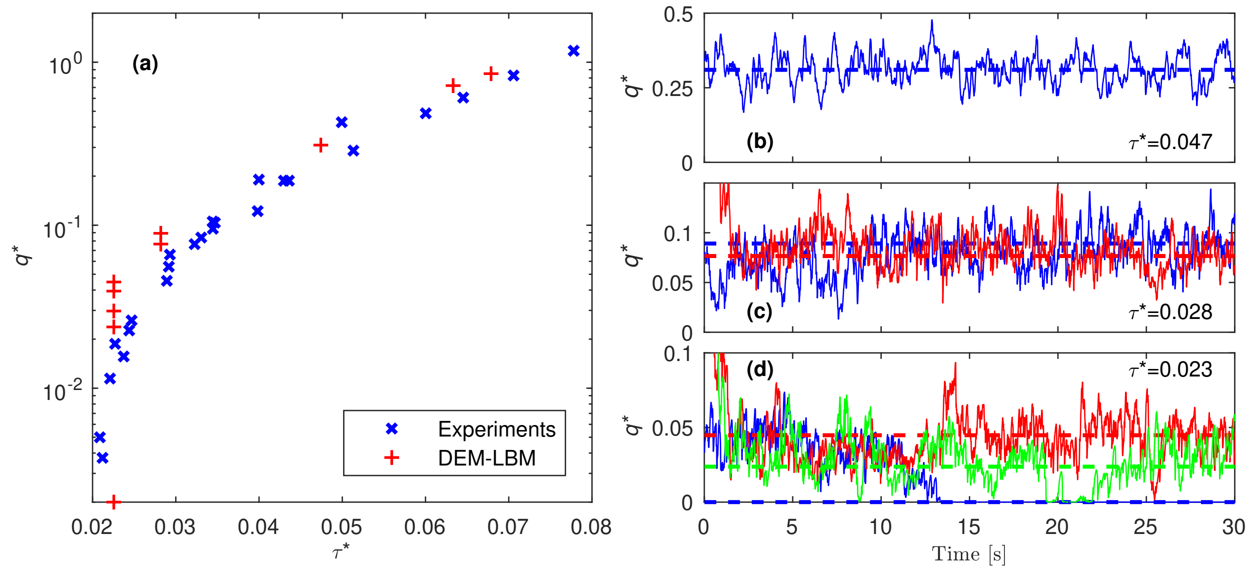

Figure 3. Dimensionless sediment transport rate q^* from DEM-LBM simulations. (a) Comparison with the q^* vs τ^* relation from experiments. The critical Shields number in the flume experiments is found to be 0.026 ± 0.002 (Benavides et al., 2021). At the lowest Shields number $\tau^* = 0.023$, the results show strong intermittency near τ_c^*. The standard initialization gives $q^* = 0$ (shown as 0.002 on the log scale), while the other four cases initialized with the steady flow fields of higher τ^* give different q^* values. Time series of q^* at (b) $\tau^* = 0.047$ (movie08 in SI), (c) $\tau^* = 0.028$ (movie06 and 07) and (d) $\tau^* = 0.023$ (showing 3 out of the 5 initializations, movie01, 02 and 05) are shown in thin curves. The thick dashed lines show the mean of the last 10s. The colors distinguish the initializations: blue–standard, red & green–steady flow of $\tau^* = 0.068$ and $\tau^* = 0.063$ respectively.

main. The resulting transport relation compared with the experimental results is shown in Figure 3(a). The standard initial condition sets the particles uniformly distributed in the whole domain with no velocity and stationary fluid. As each simulation runs, gravity drives the fluid and grains, resulting in the ultimate formation of a particle sediment bed and a transverse fluid flow profile, which transports the near surface particles. For the low Shields numbers, besides the standard initial condition just described, we also run tests where the initial particle positions and initial particle and fluid velocity are assigned from a snapshot taken at the end-phase of a higher Shields number simulation. The simulations are all carried out for at least 30s of simulation time and the last 10s of the simulations are taken to calculate the time averaged values and standard deviation of the integrated flux. The Rouse number ranges from 11.4 to 20.9, indicating the sediment transport is in the bedload regime.

Overall, in terms of the q^* vs τ^* transport relation, the DEM-LBM simulations are consistent with the experiments. At the lowest Shields number simulated, $\tau^* = 0.023$ (τ_c^* found to be 0.026$\pm$0.002 (Benavides et al., 2021)), we observe strong intermittency (see movie01 in the Supporting Information). With the standard initialization, the transport of particles eventually ceases, giving $q^* = 0$ (marked as 0.002 in Figure 3(a) due to semi-log). The additional data shown at this slope correspond to simulations using different initializations as described in the prior paragraph. Each of these tests produced low transport rates at steady state, seemingly not correlated to the flow rate of the initialization. Time series data of the transport rate for different initializations are shown in Figure 3(d). With the current sampling duration, the standard deviation of q^* at $\tau^* =$ 0.023 is on the same order of magnitude as the time averaged q^*. The fact that the variation of the sampled q^* is inversely proportional to the sampling duration (Ancey & Pascal, 2020) implies that reducing the relative uncertainty to 15% of the mean q^* at this lowest transport stage may require the simulations to be run for an additional 200s, which would be too costly for us to run. The intermittency observed could arise from internal variability or potentially from the existence of multiple attractors allowing flowing and non-flowing steady solutions to coexist at low slopes. At the second lowest simulated transport stage, $\tau^* = 0.028$, the intermittency is less obvious and the transport is continuous as shown in 3(c). The standard initialization (movie06 in SI) gives $q^* = 0.089$ with standard deviation 0.019 while the case with the fastest initialization (movie07 in SI) gives $q^* = 0.077$ with standard deviation 0.017. As τ^* increases further from the critical Shields number, the relative uncertainty of the measured q^* goes down to 16% at $\tau^* = 0.047$ (see 3(b)), 11% at $\tau^* = 0.063$ and 9% at $\tau^* = 0.068$.

One may notice that transport is observed for very low τ^* values. On one hand, we use the hydraulic radius to estimate the bed shear stress which tends to underestimate the value (J. Guo, 2015). On the other hand, a similar low threshold for sediment transport is also observed in a related experimental setup (Heyman et al., 2016) and it has been shown to not be a result of the sidewall influence on turbulence (Rousseau & Ancey, n.d.). Also as seen in the movies (Movie01 to Movie05) of the simulations, the behavior of the particles at the lowest τ^* values seems to correspond to the Intermittent Bulk Transport regime (Pähtz & Durán, 2018a) in which τ^* is above the rebound threshold but below the impact entrainment threshold, and the transported particles rebound for a relatively long period on the bed surface before depositing. Due to the periodic boundary conditions applied in the streamwise direction, the simulations have a larger autocorrelation. As a result, the simulations might overpredict q^* when particles are bounding on the bed surface.

Despite the limitation at the low Shields number, the simulations still provide microscopic details when a particle is solely entrained by the turbulent flow. In the intermittent flows shown in Figure 3(d), the green curve (corresponding to movie05 in SI) indicates that the sediment transport comes to a full stop at around 20s and then resumes at 21s when a particle on the bed surface is entrained (rolling) by the turbulent fluid.

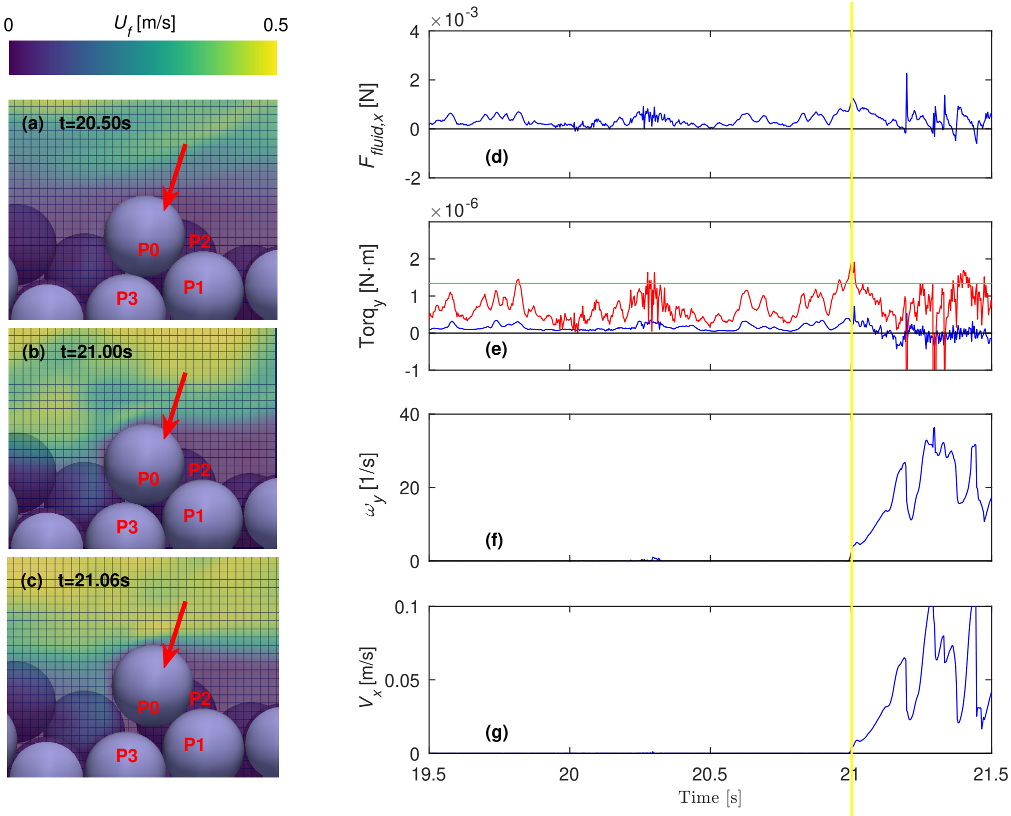

Figure 4. Examination of a near-threshold entrainment event (see movie05 in SI). (a) $t = 20.50s$, particle P0 (highlighted with red arrow) in contact with neighbors P1, P2 and P3 and the side wall. (b) $t = 21.00s$, the start of the entrainment of P0. (c) $t = 21.06s$, particle P0 gets entrained by the fluid, rolling over P1 and P2, and loses contact with P3 and the wall. Each contour shows the fluid velocity field on the plane going through the center of P0. The fluid traction over the particle surface can be treated equivalently as a single force and pure moment (couple) acting at the center of the particle. The detailed information about particle P0 around the entrainment event is displayed: (d) hydrodynamic force in the downstream direction, (e) fluid torque (blue: fluid couple, red: fluid couple + net hydrodynamic force induced torque), with respect to the hinge connecting the contact points of (P0, P1) and (P0, P2), compared with the critical torque (green) estimated by the submerged weight of P0, (f) rotational velocity (axis into the paper) and (g) downstream velocity.

As shown in Figure 4(a,b,c), the entrained particle P0 is sitting stationary on the bed surface, in contact with particle P1, P2, P3 and the side wall of the flume before 21s. Under the influence of a turbulent burst, P0 rolls over P1 and P2, losing contact with P3 and the wall.

Using DEM-LBM's capability of resolving fluid-grain traction, we now detail the processes taking place during this prototypical near-threshold entrainment event. The fluid traction over the particle surface can be treated equivalently as a single force and pure moment (couple) acting at the center of P0. Figure 4(d) shows the hydrodynamic force in the downstream direction. Figure 4(e) shows the fluid torque (into the paper component) with respect to the hinge connecting the contact points of (P0, P1) and (P0, P2). The torque is evaluated as the integration of the cross products of the lever arm vector and the hydrodynamic force vector along the surface of the particle. For reference, the green line shows the "critical" fluid torque to maintain the particle free of contact with P3 and the side wall, estimated from the submerge weight. According to Figure 4(f,g), when the fluid torque exceeds the critical value near 20.3s, P0 wiggles but still falls back. The entrainment happens at 21s when the fluid torque goes above the critical value and lasts long enough to transfer enough angular momentum to roll P0 out of the spot, which may correspond to an angular momentum criterion similar to the impulse criterion in literature (Diplas et al., 2008). The fluid torque comes from the fluid traction on the surface of P0, which is equivalent to a net hydrodynamic force on the center of P0 plus a fluid couple. The blue curve in Figure 4(e) shows the contribution of the fluid couple, which is about 1/4 of the total fluid torque (shown in red). Equivalently, the fluid traction can be simplified solely as a net force acting on the point $d_p/6$ away from the center on the far side from the hinge. The non-negligible role of the fluid couple shows that fluid-particle angular momentum transfer plays a role in the entrainment. Thus, combined fluid-DEM simulation methods that utilize only a fluid-particle drag force may be missing some relevant physics, at least at the low Shields regime. Other particles examined on the bed surface have also shown a similar $\sim 1/4$ contribution on the total fluid torque from the net fluid couple. More quantitative examinations can be found in the next subsection.

Next, we examine the flow profiles of the particles. To get the flow fields as functions of the height z with respect to the bed surface, we need to homogenize the flow fields along the flow direction and then average the profiles over time. The homogenization is carried out in three steps. The first step is to identify the particles to be used in the homogenization. In the experiments, since the motion of the particles are recorded by a camera from one side of the flume, which is slightly wider than $2d_p$, only one layer of the particles can be recognized in the images. In the post-processing of the simulations, the particles are projected onto a 2D plane which is discretized into square pixels of $d_p/25$ to mimic the images taken in the experiments. In an effort to match the experimental post-processing method, if more than 60% of the length of the perimeter is covered by particles in front of it, that particle will be labeled as invisible. For the particles left, if two projected particles are closer than $d_p/6$, only the front one is visible. The particles labeled as visible will be used in the next steps of homogenization. In the experiments, due to the refraction, the edges of the particles in the back may confuse the particle recognition in experiment images in rare cases. The resultant areal fractions can therefore be slightly different. For the bed surface, any pixel that is occupied by a particle for half a second is marked as static and then the position of the bed surface can be decided as the outline of the static pixels, as the thick black curves show in Figure 5. The vertical position z of a particle is defined as the vertical distance between the center of the particle and the bed surface. The second step is to calculate the areal fraction and particle mean velocity as functions of z. The areal fraction profile is calculated as the packing fraction of the particles labeled as visible. The velocity homogenization is obtained from the linear momentum of the layer at z. The third step is to calculate the granular temperature based on the particle-wise velocity deviation in each snapshots. More details about the last two steps of the homogenization can be found in Q. Zhang and Kamrin (2017). The images of the particles in experiments are post-processed in the same way after the particles are recognized. The fluid velocity field is also averaged temporally and spatially using a similar method to the solid velocity homogenization, based on the linear momentum of a layer of nodes at a given z.

The simulated and experimental flow profiles are very similar at a medium Shields number $\tau^* = 0.028$ and a high Shields number $\tau^* = 0.068$, as shown in Figure 5. The bed structures and the motion of the particles look similar at both Shields numbers (see movie06 and movie10 in SI). The velocity profiles match the experiments and even the granular temperature, which is a higher order variable agrees; granular temperature may be key to understanding sub-surface granular creep (Q. Zhang & Kamrin, 2017; Kim & Kamrin, 2020). The areal fraction profiles differ slightly, but are still similar to the experiment results. One reason may be that the particle recognition technique used in the experiments is not easy to replicate in the simulation post-processing, e.g., due to the refraction effects. Fortunately as long as enough particles are sampled for a given height, this difference theoretically does not change the averaged particle velocity or granular temperature; see Figure 5 (e) & (f). With the results described above, the simulations are deemed to provide a useful description of observed sediment transport processes, and we proceed to perform numerical experiments to study sediment transport problems from bulk to grain-scale.

2.3 Wide wall-free cases

We conduct a parameter study using the simulations to see what properties affect the transport rate. Namely, how much do certain details about the grains, such as particle surface friction and damping coefficient, matter versus geometric properties such as fluid depth, slope and average grain size? Wide wall-free (WWF) simulations (inspired by wide rivers, without the physical side walls like in the flumes), as shown in Figure 6(a), are a simple and useful geometry to use toward this end. The wide wall-free simulations also produce 1D solution fields and serve as benchmark cases to test the continuum modeling in Section 3.

What are the independent variables that can influence the transport rate in sediment transport problems? Putting the grain shape and size distribution aside, the variables are the gravity g, fluid density ρ_f, fluid viscosity η, slope S, water depth H, particle density ρ_s, particle diameter d_p, particle surface friction coefficient μ_p, particle damping coefficient g_p and particle stiffness k_p, which means the sediment transport rate q_s can be estimated by a ten-input function Ψ_0 as shown below:

$$q_s = \Psi_0\big(H, S, \rho_f, \eta, g, \rho_s, d_p, \mu_p, g_p, k_p\big). \tag{8}$$

The dependent (1) and independent (10) variables in Eq 8 can be non-dimensionalized by ρ_f, η and g using the below relations:

$$[\mathrm{M}] = \frac{\eta^2}{\rho_f g}, \quad [\mathrm{L}] = \left(\frac{\eta^2}{\rho_f^2 g}\right)^{1/3}, \quad [\mathrm{T}] = \left(\frac{\eta}{\rho_f g^2}\right)^{1/3}. \tag{9}$$

Since there are three dimensions involved in these 11 variables, the variables can be nondimensionlized into 8 dimensionless groups, as shown in Table 2, and the transport relation can be expressed as:

$$\Pi_0 = \Psi_1\big(\Pi_1, \Pi_2, \Pi_3, \Pi_4, \Pi_5, \Pi_6, \Pi_7\big). \tag{10}$$

We are free to operate on these dimensionless groups so that some of them become existing widely used dimensionless numbers: Π_0 can be modified into the Einstein number $q^* = \frac{\Pi_0}{\Pi_4^{3/2}(\Pi_3-1)^{1/2}}$, Π_1 into the Shields number $\tau^* = \frac{\Pi_1\Pi_2}{\Pi_4(\Pi_3-1)}$, and Π_4 into the

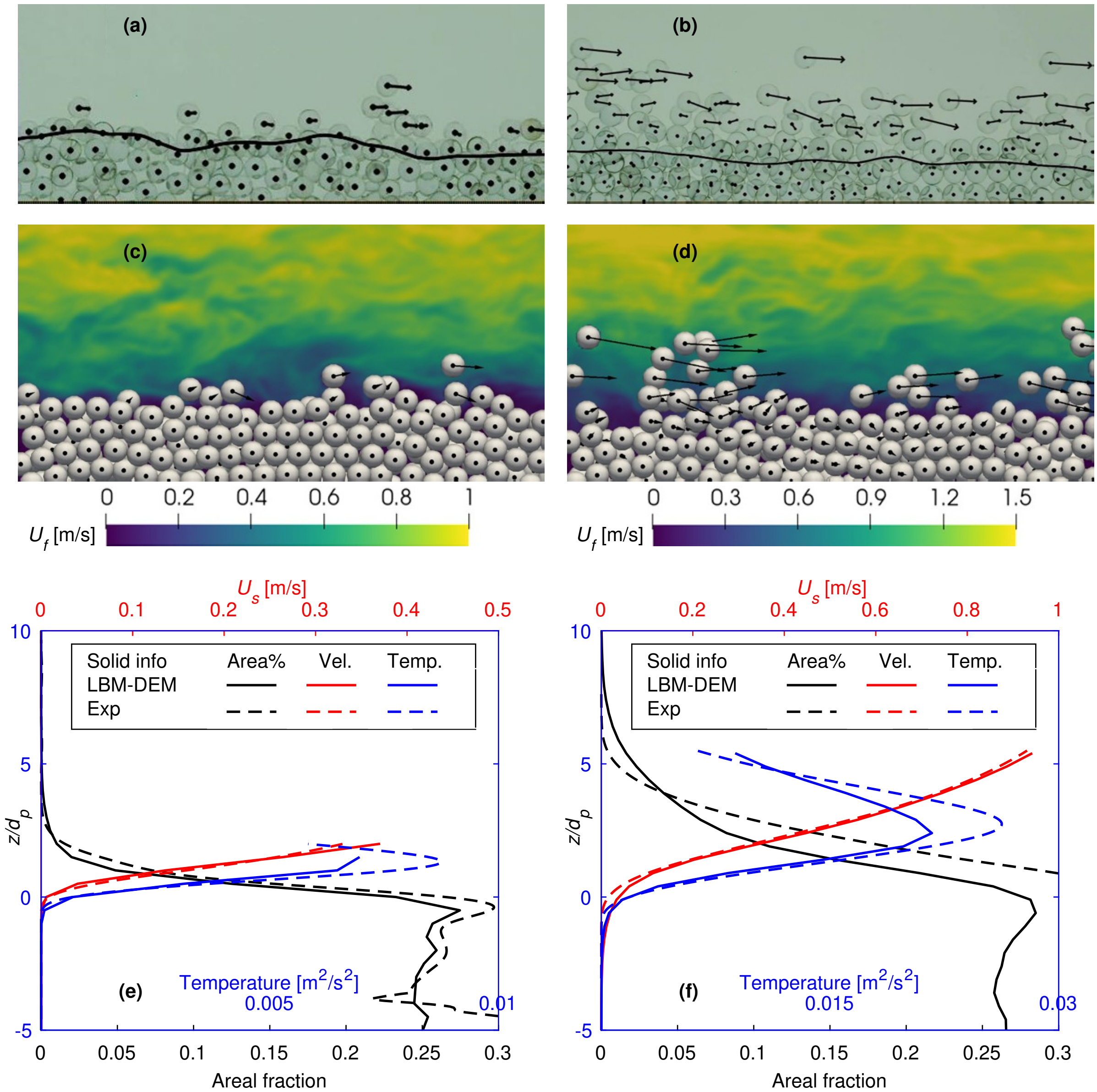

Figure 5. Comparisons between the flume experiments and DEM-LBM simulations at Shields number $\tau^* = 0.028$ (left column), and $\tau^* = 0.068$ (right column). (a) & (b) Snapshots of the flume experiments, particle in-plane velocity represented by the arrows. The black curves represent the bed surface. (c) & (d) Snapshots of the DEM-LBM simulations, particle in-plane velocity represented by the arrows, fluid field colored by the fluid velocity magnitude on the center-plane of the flume. (e) & (f) Experiments vs DEM-LBM simulations comparison in terms of the solid phase profiles as a function of the height from bed surface: areal fraction, particle velocity and granular temperature.

Table 2. Non-dimensionalization of the dependent and independent variables in sediment transport problems (Var: variables, Dim: dimensions, DN: dimensionless numbers)

Var	q_s	H	S	ρ_f	η	g	ρ_s	d_p	μ_p	g_p	k_p
Dim	$\frac{\mathrm{L}^2}{\mathrm{T}}$	L	-	$\frac{\mathrm{M}}{\mathrm{L}^3}$	$\frac{\mathrm{M}}{\mathrm{LT}}$	$\frac{\mathrm{L}}{\mathrm{T}^2}$	$\frac{\mathrm{M}}{\mathrm{L}^3}$	L	-	$\frac{\mathrm{M}}{\mathrm{T}}$	$\frac{\mathrm{M}}{\mathrm{T}^2}$
DN	$q_s\frac{\rho_f}{\eta}$	$H\left(\frac{\rho_f^2 g}{\eta^2}\right)^{\frac{1}{3}}$	S	1	1	1	$\frac{\rho_s}{\rho_f}$	$d_p\left(\frac{\rho_f^2 g}{\eta^2}\right)^{\frac{1}{3}}$	μ_p	$\frac{g_p}{\eta}\left(\frac{g\rho_f^2}{\eta^2}\right)^{\frac{1}{3}}$	$\frac{k_p}{\eta}\left(\frac{\rho_f}{\eta g}\right)^{\frac{1}{3}}$
Symbol	Π_0	Π_1	Π_2	-	-	-	Π_3	Π_4	Π_5	Π_6	Π_7

Galileo number $Ga = \frac{\sqrt{gd_p^3}}{\eta/\rho_f} = \Pi_4^{3/2}$. Also, since $\Pi_2 = S$, $\Pi_3 = \frac{\rho_s}{\rho_f}$ and $\Pi_5 = \mu_p$ are simple enough, we just use the original variables:

$$q^* = \Psi_2\left(\tau^*, S, \frac{\rho_s}{\rho_f}, Ga, \mu_p, \Pi_6, \Pi_7\right). \tag{11}$$

For sediment transport on Earth's surface, ρ_f and η are given as the values for water and $g = 9.81\mathrm{m/s}^2$. We limit our discussion to the transport of silica-based media like sand (ρ_s/ρ_f is fixed). For river bed sediment transport problems, the sand particles are in the hard limit (the particle deformation is negligible), which means $\Pi_7 \to \infty$, and thus it does not influence the transport rate. Then we have reduced the input set to five variables:

$$q^* = \tilde{\Psi}\left(\tau^*; S, Ga, \mu_p, \Pi_6\right). \tag{12}$$

Considering the empirical transport relation q^* vs τ^*, q^* can be seen as a function of τ^* parameterized by S, Ga, μ_p and Π_6 (dimensionless particle damping coefficient).

Besides the dimensionless groups above, previous researchers consider dimensionless numbers that are not included in Table 2. Here we comment on how these numbers are related to our dimensionless groups or why some of them are not included in this study. One dimensionless group commonly found in literature is the settling Reynolds number (Lajeunesse et al., 2010) $Re_s = \frac{\rho_f w_s d_p}{\eta}$ with the characteristic settling velocity $w_s = \sqrt{gd_p(\rho_s - \rho_f)/\rho_f}$, which can be written as $Re_s = Ga\sqrt{\Pi_3 - 1}$. The particle Reynolds number (Lajeunesse et al., 2010) can be written as $Re_p = \frac{\rho_f\sqrt{\tau_b/\rho_f}d_p}{\eta} = Ga\sqrt{(\Pi_3 - 1)\tau^*}$. The Rouse number (Chauchat & Guillou, 2008) can be written as $Ro = \frac{w_s}{\kappa\sqrt{\tau_b/\rho_f}} = \frac{1}{\kappa\sqrt{\tau^*}}$, where $\kappa = 0.41$ is the Von Kármán constant. Some papers (Sekine & Kikkawa, 1992; Niño et al., 1994) also use the dimensionless saltation length and saltation height, but these are actually outputs in our study and as such arise from the choice of input parameters above. Wong and Parker (2006) use the dimensionless Chezy resistance coefficient to account for the influence of the channel sidewalls, which is not necessary in this dimensional analysis for the case of wide rivers.

A new set of DEM-LBM simulations are performed without sidewalls to study the influence of the five dimensionless numbers on the sediment transport relation. The geometry of the simulated domain is shown in Figure 6(a), compared with the classical 3/2 power law. The granular bed is $24d_p$ long and $8d_p$ wide. The height of the granular bed when all the particles have settled is $10d_p$ (in total 2884 particles). The domain height is set according to the water depth H. Periodic boundary conditions are adopted at the four side boundaries. For fluid, the top boundary is a free slip boundary condition whereas the bottom is a no-slip boundary condition. The gravity is tilted by a slope S. The domain is still discretized with the grid size $dx = 0.5$mm for LBM. Simulations are performed at gentle slopes $S = 0.010$, 0.016, 0.030 with monodisperse particles whose density is $\rho_s = 2550\,\mathrm{kg/m}^3$. The simulations are in the bedload transport regime, with Rouse

Table 3. Parameters of the wide wall-free simulations. (The base parameters are red.)

Group	S	d_p(mm)	Ga	μ_p	g_p(m/s)	Π_6
WWF1	0.016	5	1378	0.5	0.09	4.2E3
WWF2	0.010	5	1378	0.5	0.09	4.2E3
WWF3	0.030	5	1378	0.5	0.09	4.2E3
WWF4	0.016	8	2789	0.5	0.09	4.2E3
WWF5	0.016	5	1378	0.1	0.09	4.2E3
WWF6	0.016	5	1378	0.5	2.11	9.8E4

number $\sim 17.4-30.0$. Corresponding to the dimensionless groups, the simulation parameters are designed to vary the dimensionless numbers one by one (as shown in Table 3) so that we can identify their influence on the q^* vs τ^* relation. The bed shear stress in this geometry can be calculated as $\tau_b = \rho_f gHS$. Water depth H is varied to set the Shields number τ^* to values ranging from 0.046 to 0.141. Each simulation is performed for 30s and the results of the last 10s are averaged, as shown in Figure 6. The averaged solid phase shear stress matches the equilibrium solution, suggesting the steady state has been reached. WWF1 is the reference group using the exact same particles as the flume tests. WWF2 and WWF3 change the macroscopic geometrical parameter S. WWF4, WWF5 and WWF6 vary the microscopic particle parameters: particle size d_p (corresponding to Ga), μ_p, and the damping coefficient g_p (corresponding to Π_6). The value in WWF6 g_p = 2.11 m/s corresponds to a dry restitution coefficient of e =0.10 while g_p = 0.09 m/s in the other groups corresponds to e =0.93. The integrated transport relation $q^*-\tau^*$ at steady state is shown in Figure 6(b) and (c).

The results of the DEM-LBM simulations from WWF1, WWF2 and WWF3 with different S overlap on top of each other, indicating S has little influence on the dimensionless sediment transport rate on gentle slopes (when τ^* is fixed) and is likely not responsible for the variation in flux (q^*) for a given Shields number (τ^*) in experiments (Meyer-Peter & Müller, 1948). The data sets with varied Ga, μ_p and Π_6 also appear very much the same as the transport relation of WWF1 as shown in Figure 6(c), except for some discrepancy at the smallest Shields number tested τ^* = 0.0471 near the threshold: smaller μ_p gives slightly larger q^* whereas larger Ga, and Π_6 give smaller q^*.

2.4 Fluid-grain torque interactions

We can also further examine the fluid-solid angular momentum transfer in the wide wall free cases. The net fluid couple (when the origin is picked at the center of the particle) exerted on the ith particle is $\boldsymbol{T}_i = \oint_{A_i} r\hat{\boldsymbol{r}}\times(\boldsymbol{\sigma}_f\hat{\boldsymbol{r}})dA$, where A_i is the surface area of the particle, $r = d_p/2$ is the radius, $\hat{\boldsymbol{r}}$ is the unit normal vector pointing out, and $\boldsymbol{\sigma}_f$ is the fluid stress tensor. The fluid traction also has a contribution to the solid phase stress tensor on the ith particle:

$$\boldsymbol{\sigma}^f_{s,i} = \frac{3}{4\pi r^3}\oint_{A_i} (\boldsymbol{\sigma}_f \cdot \hat{\boldsymbol{r}}) \otimes r\hat{\boldsymbol{r}} dA. \tag{13}$$

While the stress tensor is generally a symmetric quantity, its various contributions may not be even if the total stress still is. Here, $\boldsymbol{T}_i$ is related to the skew part of $\boldsymbol{\sigma}^f_{s,i}$ through $T_{i,l} = \sigma^f_{s,i,nm}\epsilon_{lmn}$, where ϵ_{lmn} is the 3D Levi-Civita symbol. In this study, we are most interested in the y component (into the paper) of the torque: $\sigma^f_{s,i,xz}-\sigma^f_{s,i,zx} = 3T_{i,y}/4\pi r^3$. We call $\sigma^f_{s,i,xz} - \sigma^f_{s,i,zx}$ the "rotation stress" and calculate the homogenized profile as a function of z, as shown in Figure 7(a), compared with the solid total stress, fluid stress and the packing fraction ϕ. The maximum value of the rotation stress occurs at the bed

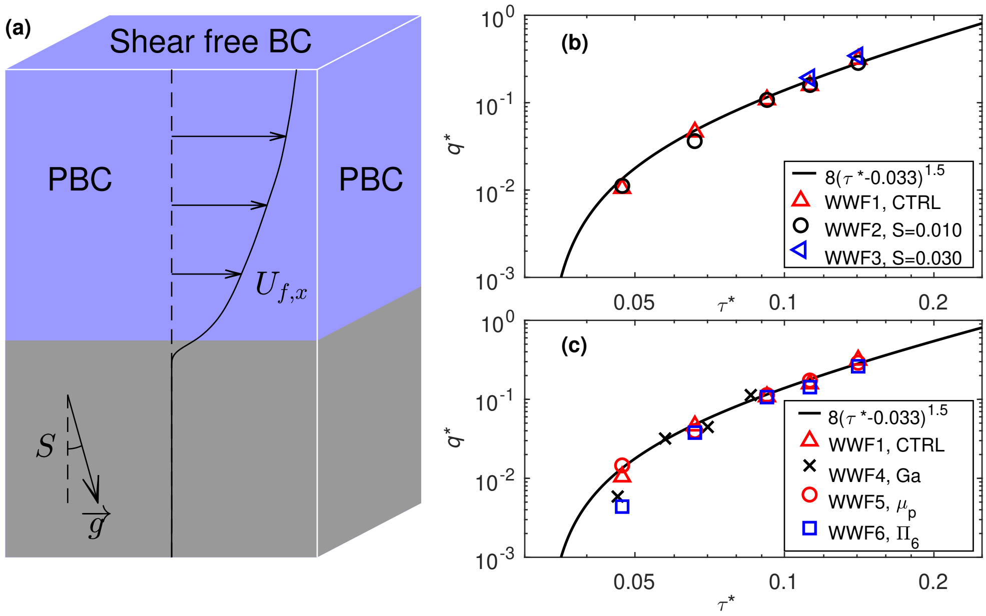

Figure 6. (a) Geometry and boundary conditions of the wide wall-free (WWF) simulations (PBC: periodic boundary condition). The simulated domain size is $24d_p \times 8d_p \times \sim 20d_p$. (b) Sediment transport relation from the wide wall-free simulations with the macroscopic geometrical parameter S varied. (c) Sediment transport relation from the wide wall-free simulations with the microscopic particle parameters Ga, μ_p and Π_6 varied. WWF1 is the control group while the other groups vary the dimensionless groups in Table 3 one by one, as denoted in the legends. The black curve is $q^* = (\tau^* - 0.033)^{1.5}$.

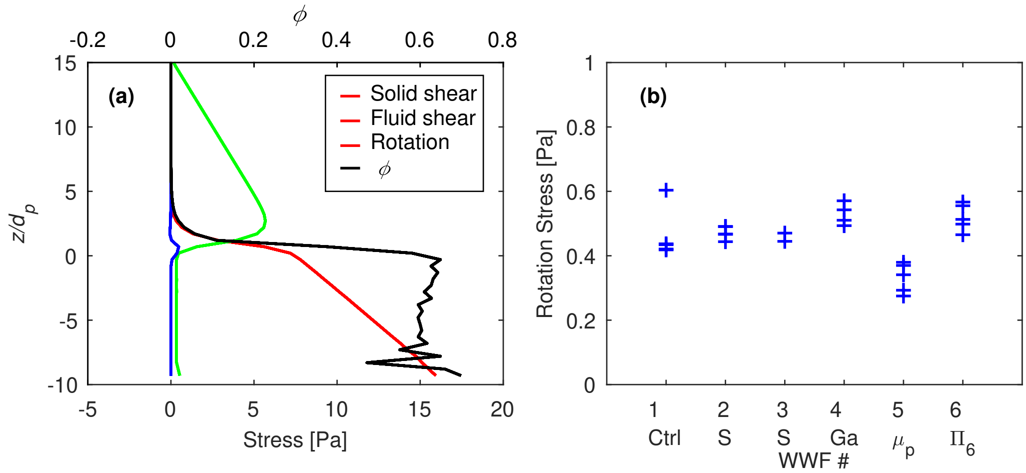

Figure 7. Examination of the rotation stress in wide wall free cases. (a) Flow profiles (WWF2 at $\tau^* = 0.085$) as a function of the height above the bed surface: solid shear stress, fluid shear stress, rotation stress and packing fraction. (b) The maximum rotation stress in different wide wall free groups.

surface, corresponding to the intuition that the exposed particles on the sediment bed surface sustain the largest fluid torque with the "help" (resistance) of the bed particles. So the rotation stress is not only a measure of the fluid torque exerted on the particles, but also an indicator of the resistive torque provided by the neighbour particles, which balance each other on average at steady state. The maximum rotation stress in the shown case is 0.47Pa, much smaller than the solid shear stress (5.62Pa) at the same position.

Figure 7(b) shows the maximum value of each rotation stress profile across different wide wall free simulation groups. Each data point comes from the profile of simulation with a unique set of physical parameters. The values from WWF1, WWF2 and WWF3 are close to each other, suggesting the slope has minor influence on the maximum rotation stress. The maximum rotation stress values of WWF4 and WWF6 are slightly higher than those in WWF1, WWF2 and WWF3, while the values of WWF5 are lower. Looking back at Figure 6(c) at the smallest Shields number $\tau^* = 0.0471$, the q^* values from different groups are inversely correlated to the corresponding maximum rotation stress in Figure 7(b) — WWF5 has the smallest rotation stress corresponding to the largest q^* while WW4 and WWF6 have larger rotation stress corresponding to smaller q^* values. Also considering that the values seem not to be correlated to the Shields number over the tested range $0.0471 \sim 0.1408$ and mostly a constant in each group, it indicates the torque resistance of the bed is like a material property of the particles. While the maximum rotation stress can be seen as a measurement of the bed resistance, on the other hand it is a driving factor for the particle motion. For the particles on the sediment bed surface, there are two driving factors countering the resistance from the neighbor particles in contact: collision with moving particles and fluid interactions (fluid net couples and hydrodynamic forces as illustrated by Figure 4). Since the maximum rotation stress is almost a constant in the tested Shields number range whereas the hydrodynamic force is correlated to τ^*, the influence of the maximum rotation stress of the material on q^* is most evident near the threshold. The maximum rotation stress of WWF5 is slightly below the control group because the low surface friction coefficient reduces the amount that particle contacts can resist the couple. In WWF6, the collisions of the particles on the bed surface dissipates more energy, which in return increases the resistance, giving rise to higher rotation stress.

3 Continuum modeling

While the DEM-LBM simulations in the last section are useful for gaining understanding, the drawback from a modeling perspective is obvious: resolving individual grains and running the LBM with a resolution of one tenth of a particle diameter makes for a method that is computationally expensive. For example, a half-minute long wide wall free simulation can take more than a week. These simulations are only affordable for small scale problems or rheological studies. For large scale problems, continuum models with proper closures can be applied for reasonable computational cost.

DEM-LBM simulations do, however, provide a prime tool for developing and extracting continuum models, offering certain advantages over experiments alone. Some of the desired experiments would be difficult to conduct in the lab setting and some of the quantities that are important in developing the continuum model are not easily accessible from experiments, such as the bulk fields of stress and velocity in the fluid and granular phase, as well as granular temperature.

In this section, we present a two-phase continuum model for steady-state behavior based on a recent mixture theory framework, turbulent-particle interaction closures, and known granular rheology principles. It is validated/calibrated directly from our DEM-LBM simulations. Close comparisons are made between the results from DEM-LBM simulations and the proposed continuum model in terms of the sediment transport relation and the detailed flow profiles of both fluid and solid phases. Besides the relatively fast motion of the transported particles and the fluid, the last subsection will also discuss the modeling of creep beneath the bed surface.

3.1 Method

A promising approach for continuum modeling of fluid-grain mixtures is to use a two-phase mixture theory (Bandara & Soga, 2015; Maurin et al., 2016; Chauchat, 2018; Baumgarten & Kamrin, 2019) that contains mass and momentum balances for both fluid and solid phases, and three closures: constitutive relations for fluid and solid phase stresses and a drag-law that transfers momentum between solid and fluid phases. As mentioned at the beginning, since the granular flow in sediment transport problems covers multiple regimes, the granular constitutive relation is crucial to making accurate predictions.

The framework of the continuum model presented here is based on a recent mixture model which spans dilute to dense regimes (Baumgarten & Kamrin, 2019), with the addition of a turbulent closure as well as an enhanced drag law and granular rheology. The solid and fluid phases of the fully immersed mixture are considered as overlapping continuum bodies with volume fractions ϕ and porosity $n = 1 - \phi$ respectively. The Cauchy stress tensor of the mixture is defined as the sum of the phase-wise Cauchy stresses: $\boldsymbol{\sigma} = \boldsymbol{\sigma}_s + \boldsymbol{\sigma}_f$. The fluid and solid phase-wise Cauchy stress can be expressed as

$$\boldsymbol{\sigma}_f = \quad \boldsymbol{\tau}_f - n\, p_f\, \mathbf{1} \tag{14}$$

$$\boldsymbol{\sigma}_s = \quad \tilde{\boldsymbol{\sigma}} \; - \phi\, p_f\, \mathbf{1}, \tag{15}$$

where $\boldsymbol{\tau}_f$ is the deviatoric part of $\boldsymbol{\sigma}_f$, $p_f = -\mathrm{tr}(\boldsymbol{\sigma}_f)/3n$ is the fluid pore pressure, and $\tilde{\boldsymbol{\sigma}}$ is the solid effective stress which drives the granular plastic flow.

The motion of the mixture in steady state is governed by the mass balance equations

$$\boldsymbol{U}_s \cdot \mathrm{grad}(\phi\rho_s) \; + \phi\, \rho_s\, \mathrm{div}\boldsymbol{U}_s \quad = 0 \tag{16}$$

$$\boldsymbol{U}_f \cdot \mathrm{grad}(n\rho_f) + n\, \rho_f\, \mathrm{div}\boldsymbol{U}_f \quad = 0 \tag{17}$$

and momentum balance equations

$$\phi\, \rho_s\, \boldsymbol{U}_s \; \cdot \mathrm{grad}(\boldsymbol{U}_s\,) \quad = \quad \phi\, \rho_s\, \boldsymbol{g} - \boldsymbol{f}_d + \mathrm{div}\tilde{\boldsymbol{\sigma}} \; - \phi\, \mathrm{grad}(p_f) \tag{18}$$

$$n\, \rho_f\, \boldsymbol{U}_f \cdot \mathrm{grad}(\boldsymbol{U}_f) \quad = \quad n\, \rho_f\, \boldsymbol{g} + \boldsymbol{f}_d + \mathrm{div}\boldsymbol{\tau}_f - n\, \mathrm{grad}(p_f), \tag{19}$$

where $\boldsymbol{f}_d$ is the drag force density from the solid phase to the fluid phase. The buoyancy is built in to the grad pressure terms.

Besides the equations of mass and momentum balances, three closures (constitutive laws) are needed to solve the system: granular rheology for $\tilde{\boldsymbol{\sigma}}$, turbulent closure for $\boldsymbol{\tau}_f$ and inter-phase drag law for $\boldsymbol{f}_d$.

3.1.1 Granular flow rule

For the steady flow of submerged granular materials, based on suspension rheological experiments, Boyer et al. (2011) proposed a rheology in which the packing fraction ϕ and granular stress ratio $\mu = \bar{\tau}/p_p$ are functions of only the dimensionless viscous number $I_v = \eta\dot{\gamma}/p_p$, where $\dot{\gamma}$ is the solid equivalent shear strain rate, granular pressure $p_p = -\mathrm{tr}(\tilde{\boldsymbol{\sigma}})/3$, and granular shear stress $\bar{\tau}$ is defined as the magnitude of the deviotoric part of $\tilde{\boldsymbol{\sigma}}$. Similarly, in the rheology of dry granular materials, ϕ and μ are solely functions of the inertial number $I = \dot{\gamma}d_p/\sqrt{p_p/\rho_s}$ (Jop et al., 2006). Trulsson et al. (2012) proposed a combination of I_v and I to unify the rheology based on 2D simulations, which covers both the viscous regime proposed for suspensions and the inertial regime when fluid resistance is minimal. Later, Amarsid et al. (2017) modified the combination as the mixed inertial number $I_m = \sqrt{2I_v + I^2}$ and expressed ϕ and μ in terms of I_m. Recently, inspired by the work of Boyer et al. (2011) and Amarsid et al. (2017), Baumgarten and Kamrin (2019) proposed a granular flow model that unifies dilute suspension rheology, dense suspension rheology, and inertial flow rheology.

Starting from the latter model, we analyze and fit the granular material parameters with additional DEM-LBM tests in simple shear geometries (Boyer et al., 2011) under varied packing fractions. In the simple shear simulations, there is no gravity and the mixture is confined between the top and bottom walls which are made of particles. The bottom wall is fixed whereas the top wall is assigned a constant horizontal shear velocity. All the side boundaries are periodic. The volume fraction of the particles is varied test-by-test from 0.03 to 0.6. The particles are exactly the same as the previous wide wall-free tests and flume tests. Instead of water, a more viscous fluid ($\eta = 0.417\,\mathrm{Pa}\cdot\mathrm{s}$) is used in the simple shear tests to avoid turbulence for now. In post-processing, $\boldsymbol{\sigma}_s$ is homogenized from the stress in each particle, which arises from grain-grain contact forces $\boldsymbol{\sigma}_s^c$, particle velocity fluctuations $\boldsymbol{\sigma}_s^{dv}$ and fluid-solid interaction $\boldsymbol{\sigma}_s^f$. The contributions from contacts and fluctuations can be calculated according to Da Cruz et al. (2005). Since DEM-LBM provides the fluid-grain momentum exchange along the grain surfaces, these can be used to calculate the fluid-force contribution to the particle-wise stress tensor (see Eq 13).

The DEM-LBM simple shear test results are shown in Figure 8, leading to an enhanced granular flow rule as follows:

$$\mu = \mu_1 + \frac{\mu_2 - \mu_1}{1 + b/I_m} + \frac{5}{2}\frac{\phi\, I_v}{a\, I_m} + \frac{5}{2}\phi\, I_v, \tag{20}$$

$$\phi = \frac{\phi_m}{1 + a\, I_m}, \tag{21}$$

where $a = \sqrt{2}/2$ is a constant and the material parameters are calibrated as $\mu_1 = 0.37$, $\mu_2 = 0.70$, $\phi_m = 0.62$, $b = 5$, as shown in Figure 8 (a,b). Eq 20 gives the solid phase stress ratio when the material is flowing ($\dot\gamma \neq 0$ or I_m, $I_v \neq 0$). When the granular material is not flowing, the solid shear stress is limited by the flow criterion: $\bar\tau - \mu_1\, p_p < 0$.

Maurin et al. (2016) have shown that the drag law in bedload transport problems can be fitted by the $\mu(I)$ rheology which is originally for dry granular materials. In our cases as well, the dry inertial number I dominates the mixed inertial number $I_m = \sqrt{2I_v + I^2}$ with the ratio $I^2/2I_v = \dot\gamma d_P^2/2\nu$ greater than 10 above the bed surface. We find the last two terms of Eq 20 contribute less than 5% to the value of μ for $\phi > 0.05$; these terms serve primarily to recover the suspension effective viscosity in the dilute limit. As shown in Figure 8(c), the I_m based rheology predictions for the bedload flow are still consistent with the DEM-LBM results. In contrast, Figure 8(d) shows the $\mu(I)$ relation is consistent with the bedload data, but does not match the rheological simple shear tests when $I^2/2I_v$ is low. In this two-phase framework, we choose to use the more universal $\mu(I_m)$ relation because it can be generalized more easily to suspended load in sediment transport or even other particle laden flow scenarios, as suggested by Baumgarten and Kamrin (2019). Note that neither rheology predicts the observed behavior for $\mu < \mu_1$ in Figure 8(c,d), which are caused by nonlocal effects, which will be modeled in an upcoming section.

The last term in Eq 20 for the solid phase stress was previously attributed to the fluid shear stress in (Baumgarten & Kamrin, 2019). We have some freedom in choosing which phase includes this contribution — the phase-wise stress decomposition is not totally known. Its placement does not affect the total stress nor the model's ability to span dilute suspensions, dense suspensions, and dry granular flows (see Baumgarten and Kamrin (2019) for more details about how these regimes are recovered). That said, it is reasonable to include as part of the solid stress since it induced by fluid traction on the grains and Eq 20 matches our DEM-LBM data more closely.

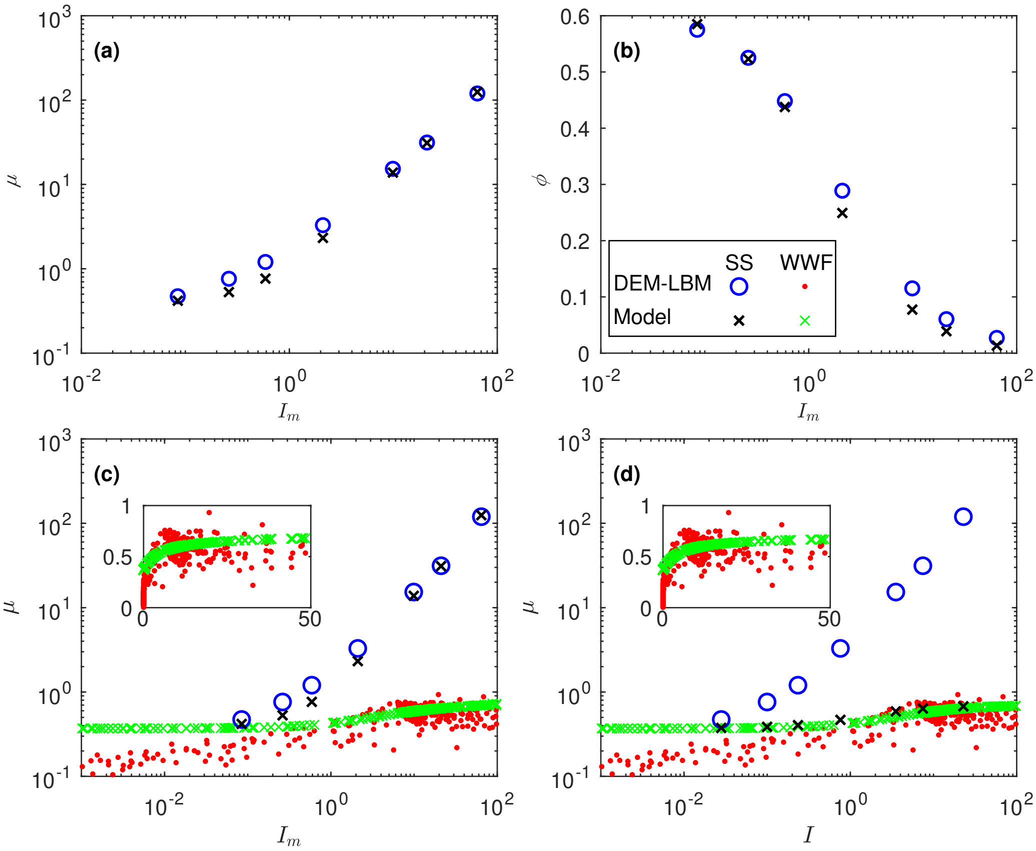

Figure 8. Granular flow rule from simple shear SS simulations: (a) the dependence of stress ratio μ on the mixed inertial number I_m, (b) packing fraction ϕ as a function of I_m. Fitted granular flow rule validated with the data from the wide wall free (WWF) simulations: (c) Scatter plot of μ versus I_m , (d) scatter plot of μ and I (dry rheology). Each data point of DEM-LBM comes from a set of homogenized values at a elevation in a WWF test (in total 27 included).

3.1.2 Turbulent closures

Turbulence in the fluid produces Reynolds shear stresses and turbulent effects on particle drift, which can both influence sediment transport. The Reynolds shear stress can be modeled using mixing length models (L. Li & Sawamoto, 1995; Revil-Baudard et al., 2015; Berzi & Fraccarollo, 2015). Here we use that of (Berzi & Fraccarollo, 2015) where the mixing length is fully determined by the local granular packing fraction ϕ without integrating or calculating the distance from the bed surface, which can be challenging in complex 2D or 3D cases. The turbulent viscosity is modeled as

$$\eta_t = n\, \rho_f\, l_m^2\, ||\boldsymbol{D}_{0f}||, \tag{22}$$

with the mixing length formulated as

$$l_m = 3\, d_p\, (\phi_m - \phi)^3. \tag{23}$$

ϕ_m is the random close packing fraction of the particles which is $\phi_m = 0.62$ for the DEM grains. The deviotoric part of the fluid stress is then calculated as $\boldsymbol{\tau}_f = 2(\eta + \eta_t)\boldsymbol{D}_{0f}$. Experiments (Ni & Capart, 2018) have shown $l_m/d_p \geq 0.2$ is a lower limit of the mixing length at high packing fraction, where wake effects dominate the vertical mixing of momentum, so we use $l_m/d_p \geq 0.2$ as the lower bound of Eq 23.

Due to the velocity fluctuations of the turbulent flow, the particles experience an additional drift velocity $\boldsymbol{u}_d$ (Simonin, 1989), which is crucial to recover the Rouse profile (Rouse, 1937) in sheet flows Chauchat (2018). Here we formulate the model in a general vectorial form:

$$\boldsymbol{u}_d = -\frac{\eta_t}{\rho_f\, \Sigma_s\, \phi}\, \mathrm{grad}\phi, \tag{24}$$

where Σ_s is the turbulent Schmidt number and has been shown to be a constant above a certain height from the bed surface in the sheet flow (Chauchat, 2018). When implemented into a two-phase solver, we use $\Sigma_s = 0.3$.

3.1.3 Drag law

The interphase drag force density $\boldsymbol{f}_d$ can be modeled using the common drag form

$$\boldsymbol{f}_d = \frac{18\phi(1-\phi)\eta}{d_p^2} F(\phi, Re_d)\, \Delta\boldsymbol{U}. \tag{25}$$

For turbulent flows, the velocity difference above is modified to account for turbulent drift as $\Delta\boldsymbol{U} = \boldsymbol{U}_s - \boldsymbol{U}_f + \boldsymbol{u}_d$. The function $F(\phi, Re_d)$ is the dimensionless drag function with $Re_d = (1-\phi)\rho_f||\Delta\boldsymbol{U}||/\eta$. The Stokes drag law for a single sphere implies $F(0,0) = 1$. One typical way to determine $F(\phi, Re_d)$ is to measure $F(0, Re_d)$ with a single particle and then account for hindrance effects from neighbouring particles, such as the Schiller (1933) model:

$$F_1(\phi, Re_d) = F(0, Re_d)(1-\phi)^{-1-h_{\mathrm{Exp}}}, \tag{26}$$

where the exponent h_{Exp} is taken as a constant value of 2 in a recent work on the continuum modeling of sediment transport (Chauchat et al., 2017) and the expression for $F(0, Re_d)$ is evaluated as $1 + 0.15 Re_d^{0.687}$ for $Re_d \leq 1000$ and $\frac{0.44}{24} Re_d$ for $Re_d > 1000$. Alternatively, $F(\phi, Re_d)$ can also be determined in the Stokes flow limit as $F(\phi, 0)$ and then extended by adding a term related to Re_d. For example, Beetstra et al. (2007) proposed the expression below from fitting

$$F_2(\phi, Re_d) = \frac{10\phi}{(1-\phi)^2} + (1-\phi)^2(1 + 1.5\sqrt{\phi}) + \frac{0.413 Re_d}{24(1-\phi)^2}\left(\frac{(1-\phi)^{-1} + 3\phi(1-\phi) + 8.4 Re_d^{-0.343}}{1 + 10^{3\phi} Re_d^{-(1+4\phi)/2}}\right). \tag{27}$$

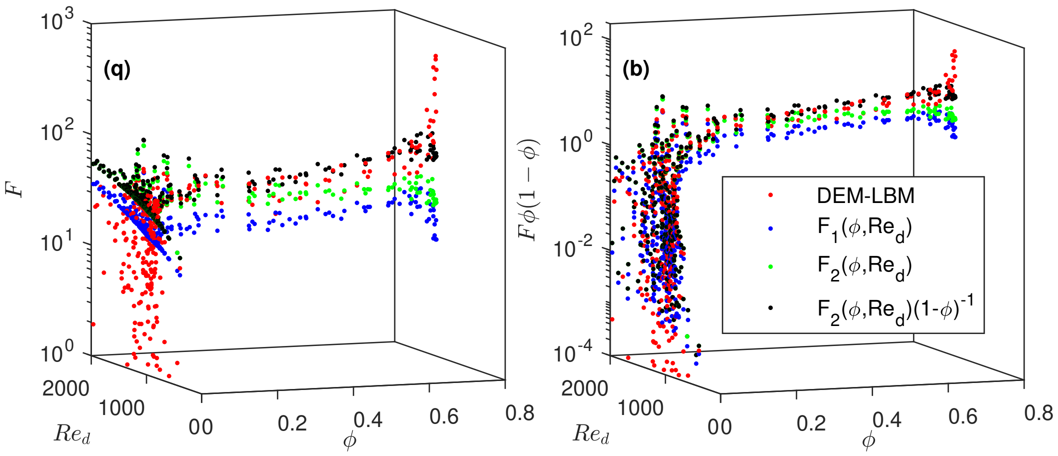

Figure 9. Comparison of different dimensionless drag coefficient formulas $F_1(\phi, Re_d)$, $F_2(\phi, Re_d)$ and the modified $F_2(\phi, Re_d)(1 - \phi)^{-1}$ against the DEM-LBM results: (e) The dimensionless drag coefficient F as a function of ϕ and Re_d. (f) $F\phi(1 - \phi)$ as a function of ϕ and Re_d. The formulas are evaluated at the same ϕ and Re_d values as the DEM-LBM data. F_1 and F_2 tend to underestimate the drag whereas $F_2(\phi, Re_d)(1 - \phi)^{-1}$ gives better fitting. Each data point of DEM-LBM comes from a set of homogenized values at an elevation in a WWF test (in total 27 included).

The data from DEM-LBM simulations can serve as a tool to test/validate these two drag laws. The drag force density can be extracted from the net fluid force per particle in our DEM-LBM wide wall-free simulations, and then homogenized layer-wise at each z and averaged over time to produce F. Similarly, ϕ and Re_d can be homogenized layer-wise. The measured dimensionless drag coefficient is compared with the predictions of F_1 and F_2 evaluated at the same ϕ and Re_d values, as shown in Figure 9(a). According to Eq 25, F will be multiplied by $\phi(1-\phi)$ when used to calculate the drag force density $\boldsymbol{f}_d$, so the comparison of $\phi(1-\phi)F$ is also included in Figure 9(b). F_1 and F_2 tend to underestimate the drag because Eq 26 and Eq 27 arise from considering a fluid flowing through a fixed, isotropic array of grains. When it comes to mobile particles in sediment transport problems or fluidized granular beds, the actual drag forces are claimed to be higher than this relation due to granular velocity fluctuations (Wylie et al., 2003; Kriebitzsch et al., 2013), packing heterogeneity (Derksen, 2014), and/or packing anisotropy (Holloway et al., 2012; Ma et al., 2020). We account for this effect as follows. The agreement presented in the single sphere settling tests, as shown in Appendix B, indicates that $F_1(0, Re_d)$ should be recovered in the DEM-LBM simulations. Thus, a simple way to modify the drag law but keep this limit is to multiply $F_1(\phi, Re_d)$ or $F_2(\phi, Re_d)$ above with a correction that is a power of $(1-\phi)$ as an hindrance coefficient (Richardson & Zaki, 1954; Di Felice, 1994). We find the error of the drag law in our system can be reduced by choosing the additional factor to be $(1-\phi)^{-1}$, i.e.,

$$F(\phi, Re_d) = F_2(\phi, Re_d)(1-\phi)^{-1}. \tag{28}$$

The proposed formula F fits the DEM-LBM results better than the original formula F_2 for fixed grain arrays.

3.2 Wide wall-free cases

The continuum model with the calibrated material parameters described above has been implemented in a 1D two-phase solver to model the wide wall-free cases. The equa-

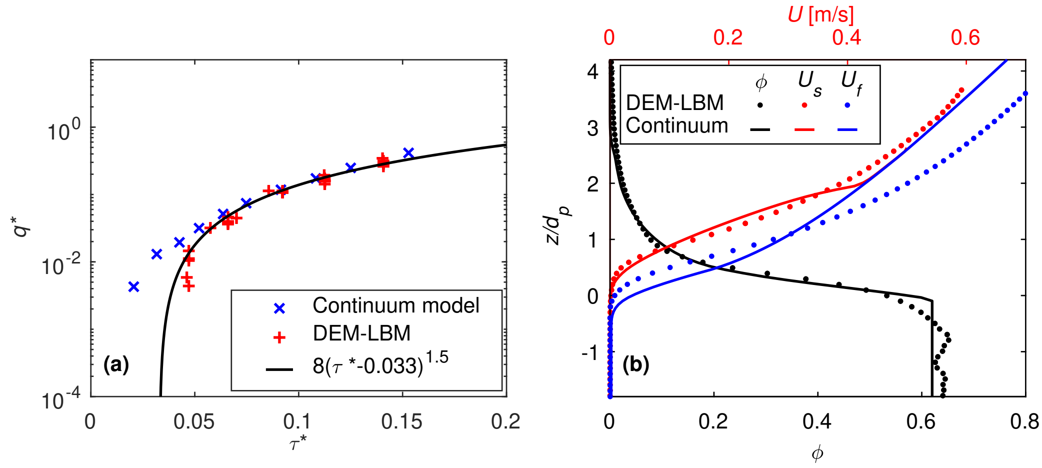

Figure 10. Comparison between DEM-LBM simulations and the continuum model for the wide wall-free geometry: (a) sediment transport relation, and (b) flow profiles (WWF2 at $\tau^* = 0.085$) as a function of the height above the bed surface: fluid velocity, solid velocity and solid packing fraction.

tions are solved with transient terms and a granular dilation rule (Pailha & Pouliquen, 2009) using the finite volume method. When the steady state is reached, the transient terms and dilation rule vanish so that the solution is not influenced.

The wide wall-free cases are solved with a given slope S and varied water depth H. The transport relation from multiple solutions is shown in Figure 10(a). Each data point represents a single solution for a given H or τ^*. The transport relation from the continuum model matches with that from DEM-LBM simulations, giving a good fit to the widely used (albeit flawed) 3/2 power law. Figure 10(b) shows the comparison of the flow profiles from continuum modeling and DEM-LBM simulations. The modeled solid packing fraction profile ϕ matches the simulation almost exactly and the solid velocity profile also matches .

One difference in Figure 10(b) is that the solution of the continuum model predicts $\boldsymbol{U}_s$ and $\boldsymbol{U}_f$ to merge into the same profile for $\phi < 0.05$ by observation while in DEM-LBM $\boldsymbol{U}_s$ is always lagging behind $\boldsymbol{U}_f$. The reason for this deviation is that in the DEM-LBM simulations the very top layer of the particles in the dilute suspension always come up from the granular flow below and they are always slower than the local ambient fluid flow (accelerating streamwise all the way up). On the other hand, there is no such vertical momentum mixing effects (in steady state) in our current continuum model. Moreover, $\boldsymbol{u}_d$ predicted by the continuum model is large enough for the lift force to cancel out the submerged weight of the solid phase, so that the local un-pressurized solid phase sustains no shear stress and co-moves with the fluid phase. For the granular material governed by a frictional flow rule, $p_p = 0$ means the material is suspended and free to be sheared. As a result, there is no drag force in the flow direction (so no velocity lag) for the very dilute layers. For a remedy, there are two future research directions: (1) enhancing the drift velocity formula so that the submerged weight does not fully cancel out, or (2) a granular flow rule for the very dilute regime that considers the vertical mixing of solid phase momentum due to the granular temperature, packing fraction gradient, velocity gradient, and perhaps the gradient of the velocity gradient. Another problem is the abrupt transition to the maximum concentration near bed surface, resulting from the previously mentioned granular flow rule with a flow criterion given by μ_1. The kink corresponds to the elevation where $\mu = \mu_1$, which gives $\phi = \phi_m$ and $\dot{\gamma} = 0$ for all the points below it. Incorporating a nonlocal rheology into the two-phase model may improve the solution near and below the bed surface. As mentioned previously, the drag force density on mobile sheared particles is larger than that on fixed randomly packed particles. More analytical work on this would shed light on the interaction between fluid and solid phases in such flow problems. Finally, we note that this model, which utilizes a standard mixture theoretic decomposition of the stress, is not equipped to model the details of the different stress contributors in each phase beyond the splitting shown in Eqs 14 and 15. A higher order mixture model could incorporate a micropolar form for the different contributions (Cosserat & Cosserat, 1909; Kamrin, 2019) to permit counterbalancing rotation stresses within each phase to account for the near-bed-surface behavior in Sec 2.4, which can be a future research direction.

3.3 Creep modeling

For the very dense flow region $\phi \sim \phi_m$ under the bed surface, creep flow (exponential decay of $\boldsymbol{U}_s$) is also observed in DEM-LBM simulations, which is known to be driven by nonlocal effects arising from finite grain size (Silbert et al., 2003; Mueth, 2003; Bonnoit et al., 2010). Creep flow is not contributing much to the $q^*{-}\tau^*$ transport relation for τ^* far from τ_c^*. However, its effect can matter over the long term, e.g. creep may lead to vertical grain size sorting in river beds (Ferdowsi et al., 2017), and thus accurate modeling of the creeping flow could be helpful to predict river bed armouring.

In the creep zone, the velocities of the particles and the fluid, as well as the relative velocity between the two phases, are so small that the drag forces and lubrication forces from fluid are tiny. One may wonder, hence, if a rheology for the creep of dry granular materials will also work here. We consider the Nonlocal Granular Fluidity model (NGF) (Kamrin & Koval, 2012; Kamrin & Henann, 2015), which is able to model creep flow in dry granular materials in many cases. In the NGF constitutive model, a phase field called the fluidity, g, is postulated to exist, which satisfies the dynamical partial differential equation:

$$t_0\dot{g} = A^2 d_p^2 \nabla^2 g - (\mu_2 - \mu_1)\left(\frac{\mu_1 - \mu}{\mu_2 - \mu}\right) g - b\sqrt{\frac{\rho_s d_p^2}{p_p}}\mu g^2 \tag{29}$$

where the nonlocal amplitude $A = 0.43$ is a dimensionless constant given by the grain geometry and t_0 is a time-scale. The fluidity then directly controls the stress-flow rheology by the relation $\dot{\gamma} = g\mu$. The "unexpected" flow (i.e. creep) of the solid phase in the region where the load is below the local flow criterion comes from the diffusion term in Eq 29, which is scaled directly by the grain size d_p. Recent research (Q. Zhang & Kamrin, 2017; Kim & Kamrin, 2020) shows that g is very likely to be related to the velocity fluctuations of the particles. Thus, the physical picture for the creep flow is as follows: the high granular temperature region of fast flow at the bed surface is a source of g that diffuses downward and "warms up" the cold zone deeper into the bed so that it too can flow. The NGF model parameters are usually fitted from the inertial flow rule for dry granular materials mentioned in 3.1.1. Equation (18) then closes the system of equations.

We solve the NGF model in the wide wall-free flow geometry with some aid from the DEM-LBM results. Since Eq 18 needs the fluid forcing, $-\boldsymbol{f}_d{-}\phi\,\mathrm{grad}(p_f)$, which is not computed from NGF, we simply extract this field directly from the fluid forces in the corresponding DEM-LBM simulation. The g field also needs reasonable boundary conditions. We set $g = 0$ at the bottom of the bed ($z = -10d_p$) and set the g value at $z = -2d_p$ from DEM-LBM tests (using $g = \dot{\gamma}/\mu$) at $z = -2d_p$. Then the velocity of the solid phase can be integrated from the fixed bottom using the solved g field. Figure 11 gives the solid phase velocity profile comparison between the DEM-LBM wide wall-free simulation (d_p=5mm, $S = 0.016$) and the corresponding steady state NGF solution. The NGF result shows an exponential decay with a decay length of $\sim 2.5d_p$, in

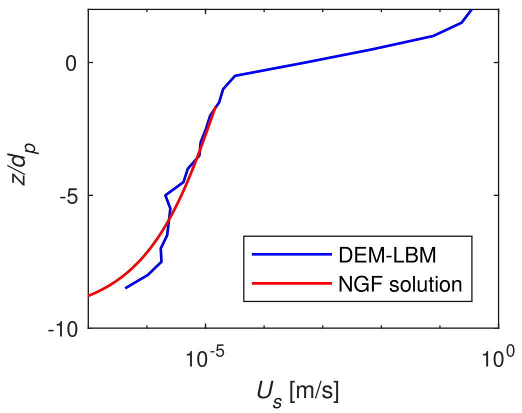

Figure 11. The solid phase velocity profile comparison between a DEM-LBM wide wall-free simulation (d_p=5mm, $S = 0.016$) and the corresponding steady state NGF solution.

agreement with our DEM-LBM results as well as separate experimental measurements from immersed sediment beds (Allen & Kudrolli, 2017) and dry granular beds (Siavoshi et al., 2006) in similar geometries. This confirms our expectation that the minimal effect of fluid in the deeper zones causes the material to creep as a dry media would.

4 Discussion

With regard to the motivating questions asked in the introduction, our study provides the following outlook.

4.1 How important is fluid-particle angular momentum transfer and in which part of the flow and in which regime of the sediment transport is it important?

Our simulations resolve the fluid traction over the particle surfaces, leading to a hydrodynamic net force on the center of each particle along with a fluid net couple. Examination of particles entrained by fluid on the bed surface in intermittent sediment transport flume simulations show that nearly 1/4 of the total fluid torque to roll over neighboring grains comes from the net fluid couple, which is non-negligible especially near the transport threshold. In each wide wall free simulations, the rotation stress, which measures the skewness of the fluid-imposed stress contribution in a grain, seems to be concentrated near the sediment bed surface where it is balanced by the torque resistance arising from the enduring contact with other bed particles. The maximum rotation stress seems not correlated to the Shields number (in the tested range from 0.0471−0.1408), which can be seen as a material indicator of how much fluid net couple the sediment bed can sustain (on the other hand, it is part of the hydrodynamic driving). On the other hand, the fluid net force per grain appears correlated to τ^*. As a result, the influence of the fluid net couple (or the defined rotation stress) is most evident for $\tau^* \to \tau_c^*$ and is negligible for $\tau^* \gg \tau_c^*$, which is shown in this study in terms of the sediment transport relation. This analysis suggests fluid-DEM simulation methodologies that do not explicitly model the small scale fluid-grain interaction may need to use a closure for the angular momentum transfer, such as in Finn et al. (2016) and Guan et al. (2021), especially when close to the sediment transport threshold.

4.2 What is (not) responsible for the variability in the observed sediment transport relation?

The dimensional analysis and the relevant parameter space exploration with DEM-LBM simulations lead to several conclusions, though limited to the simplest geometry (a infinite long and wide straight river) without considering vegetation or external agitation. In terms of macroscopic factors, the bed slope has little influence on the dimensionless sediment transport rate on gentle slopes (when τ^* is fixed) and is likely not responsible for the variation in flux (q^*) for a given Shields number (τ^*) in experiments (Meyer-Peter & Müller, 1948). This is not a surprise, in agreement with recent theoretical works (Maurin et al., 2018; Pähtz & Durán, 2020) about the influence of (steep) slopes on the transport relation, which give correction factors of q^*, τ^* and τ_c^* very close to 1 for gentle slopes ranging from 0.01 to 0.03.

In terms of microscopic particle properties on which this study focuses, tests that independently varied the mean particle size, surface friction coefficient, and surface damping coefficient do not appear to produce transport relations that differ much compared to the reference case at medium to high transport stages. When it is close to the transport threshold, the q^* values in these different simulation groups seem to be inversely correlated to the rotation stress which is correlated to the surface friction coefficient and damping coefficient of the particles.

Following the previous logic regarding the competition between driving factors to dislodge bed particles (collisions and interactions with fluid) countering the resistance from the contact interactions, if we look back at the factors we isolated at the beginning of this analysis, the grain shape (Kock & Huhn, 2007; Pähtz et al., 2021) as well as the hydrodynamic interaction (Camenen, 2007), and size distribution (including effects such as small particles hiding behind large neighbors), may have contributions to the variation in the transport relation. From a different perspective, large particles on river beds also control morphological stability (MacKenzie & Eaton, 2017; MacKenzie et al., 2018), which is possibly another reason. This agrees with the findings of the companion experimental work (Deal et al., 2021), in which the $q^*-\tau^*$ relation is parameterized primarily by the repose angle of the sediment particles and the ratio of the effective drag coefficient to the drag coefficient of the volume-equivalent sphere. Though the particle surface friction coefficient μ_p influences the repose angle, the influence for round particles is very limited when $\mu_p > 0.05$ (Walton, 1994; Wiacek et al., 2012; Kamrin & Koval, 2014), consistent with the fact that μ_p has a minor influence on the value of the maximum rotation stress. As a result, μ_p has negligible influence on the transport of spherical sediment particles, but may potentially have more influence on the transport of non-spherical particles.

Besides the microscopic particle properties, other factors that may also play important roles in the variation of the transport relation include the presence of external agitation (Sumer et al., 2003; Ojha et al., 2019; Cheng et al., 2020) and vegetation (Vargas-Luna et al., 2015; C. Liu et al., 2021). It should also be noted that here we have only considered the case of simple channel geometry, whereas in actual riverbeds there are a number of channel morphologic features we have not considered that can make a difference, including bedforms (Parker, 1978) and the ratio of grain diameter to flow depth, especially if boulders are present that are not fully submerged (Yager et al., 2007; Venditti, 2013; Venditti et al., 2017).

4.3 How can we formulate a useful, broadly applicable model at different scales and regimes in bedload sediment transport?

The two-phase continuum framework shown here can be used to predict the bedload transport relation with proper closures: a granular flow rule, a turbulent closure, and a drag law. The transport relation predicted by the model in the wide wall-free cases matches with that from DEM-LBM simulations, giving the classical power law of 3/2. The modeled solid packing fraction profile matches the simulation almost exactly and the solid velocity profile also matches .

For creep flow beneath the bed surface, the success of the NGF model, which has previously been used for dry media, suggests that the physics of cooperative grain motion giving rise to creep in fluid-submerged dense packings may be similar to that in dry packings. In our implementation here, drag forces from the fluid were homogenized from DEM-LBM simulations and applied to the NGF domain as a body force and the fluidity value is specified on the top as the boundary condition. Note that the NGF model does not require $\mu > \mu_1$ anywhere for non-zero flow to exist. As long as there is a finite fluidity boundary condition, flow can happen all beneath μ_1. For example, the presented solution in Section 3.3 is obtained by solving the solid field in the creep zone $z \leq -2d_p$ with $\mu < \mu_1$ everywhere. Finite fluidity occurs at the bed surface even if $\mu < \mu_1$ there because the turbulent fluid imparts fluctuations to the bed surface particles resulting in a fluidity source. This interpretation utilizes the result in Q. Zhang and Kamrin (2017) that shows fluidity is in fact a measure of grain fluctuations, so any agency that imparts grain fluctuations can be a source for fluidity in a granular system. We have inferred the fluidity boundary condition from the DEM-LBM simulations, but in principle one could identify a model for the fluidity boundary conditions that depends on the turbulence. In the future we could extend the granular rheology used in our two-phase mixture model to incorporate NGF in the creeping regime, so that fluid flow and granular flow fields are simultaneously computed down to the creeping flow regime.We also acknowledge that creep flows can happen when μ is below μ_1 everywhere (Houssais et al., 2015; Allen & Kudrolli, 2018), the boundary values may be what we want to predict instead of an input. See the review paper (Pähtz et al., 2020) for more insights.

The continuum tools we have used make a number of direct ties to the particle-scale information, which can be exploited to apply the model to other bed materials. For example some of the parameters in the drag law at the dilute limit can be calibrated with single particle settling tests. The critical stress ratio μ_1 can be approximated by the static angle of repose of the grains (even if dry). Other parameters in the granular flow rule can be calibrated with basic flow tests. For example, the nonlocal amplitude used in the creep flow model can be inferred from the decay length of the mean particle velocity in wall-bounded chute flows (Komatsu et al., 2001; D. Liu & Henann, 2017) or from annular Couette flow tests (Kamrin & Koval, 2012, 2014).

5 Conclusion

In this paper, sub-grain scale resolved DEM-LBM simulations of mono-disperse spherical sediment particles were performed and the results compared closely with data from flume experiments. The simulations was shown to match the experiments in terms of the transport relation and the detailed flow profiles of the granular material. With validation in hand, the DEM-LBM tool was then used as the basis for an in-depth modeling study of sediment transport. Wide wall-free simulations were performed in order to evaluate the factors that can potentially affect the transport relation on gentle slopes ($0.01 \sim 0.03$). The slope, the mean particle size, the surface friction coefficient, and the damping coefficient did not appear to influence the dimensionless transport rate for medium to high Shields number when the Shields number was fixed, for spherical sediment particles. Instead, the parameters not included in the dimensional analysis may be responsible for a substantial fraction of the variability in the experimental transport relation on gentle slopes, including particle parameters such as the particle shape and size distribution as well as vegetation, external agitation, bed forms and so on. The particle-resolved simulations also provided details about the fluid-particle angular momentum exchange. The fluid couple with respect to the center of the grain, resulting from the fluid traction over the particle surface, was shown non-negligible for the fluid entrainment near the threshold. The fluid couple was further quantified as the rotation stress, which was found mostly concentrated near the bed surface and not correlated to the Shields number. Particle properties (e.g. surface friction coefficient) changed the observed rotation stress, which was anti-correlated to q^* near the transport threshold, suggesting fluid-particle angular momentum transfer may play a role in transport behavior near the threshold.

Appendix A Wall boundary condition for flume tests (boundary layer treatment)

To ensure the fluid velocity in the DEM-LBM simulations, it is correct is crucial to recover the transport relation of the sediment particles. In the flume experiments (Deal et al., 2021; Benavides et al., 2021), the flumes are narrow and tall so that the cross-sectional fluid streamwise velocity far from the granular bed can be approximated by the law of the wall when fully developed. According to the law of the wall, the velocity near the wall (viscous sublayer, $y^+ < 10.8$) is linear to the wall distance $u^+ = y^+$ with $y^+ = y_w u_\tau/\nu_f$, $u_\tau = \sqrt{\tau_w/\rho_f}$ and $u^+ = u/u_\tau$, where y_w is the distance to the closest wall of the channel and τ_w is the wall shear stress. Beyond the viscous sublayer, the fluid average velocity not too close to the walls ($y^+ \geq 10.8$) can be formulated as $u^+ = \ln y^+/0.41 + 5.0$. The goal of this appendix is to explain how we can recover the turbulent pure fluid cross-sectional velocity profile in the channel without having to directly resolve the boundary layer.

LBM has shown the capability to simulate homogeneous isotropic turbulent flows accurately (Yu et al., 2005), either on a high resolution mesh whose grid spacing is no larger than Kolmogorov length scale δx_K (as known as Direct Numerical Simulations or DNS), or a relatively coarse mesh with a turbulent closure (LES). Various papers on LBM (Banari et al., 2015; L. Wang et al., 2016; Eshghinejadfard et al., 2017) have shown DNS can recover the turbulent fluid velocity profile in a channel with two parallel walls. However in LBM with LES such as our simulations, the thickness of the viscous sublayer of the boundary layer is smaller than or comparable with the grid spacing dx, leading to a velocity jump near the boundaries. LBM based LES with a no-slip boundary condition will underestimate the fluid velocity in the channel. Here, we present a new boundary technique, relating the velocity jump across the boundary layer as a slip velocity in a Navier slip boundary condition formulation.

Uth et al. (2013) and K. Wang et al. (2018) have provided the implementation method of the Navier slip boundary condition in LBM. The slip boundary condition is characterized by a scalar s_{sl}, the slip length defined as the distance from the wall at which the linearly extrapolated relative velocity is 0. At the boundary, if f_i corresponds to the oblique velocity $\boldsymbol{c}_i$ going into the wall, the distribution component coming out of the wall in the opposite direction can be made up as

$$f_{i'}(\boldsymbol{x}_w, t+1) = r_1\, f_i^c(\boldsymbol{x}_w, t) + (1-r_1)\, f_{i'''}^c(\boldsymbol{x}_w, t) \tag{A1}$$

with

$$r_1 = \frac{1}{1 + \frac{s_{sl}}{dx\,(\tau - 1/2)}} \tag{A2}$$

where $f_{i'''}$ corresponds to the velocity going into the wall in the specular reflection direction (the opposite direction of $\boldsymbol{c}_{i''}$, see Figure 1 (c)) and the superscript "c" denotes the post-collision distribution. Substituting Eqn (4) and $s_{sl} = u_{sl}/\dot{\gamma}_{f,w}$ gives

$$r_1 = \frac{1}{1 + \frac{u_{sl}}{\dot{\gamma}_{f,w}\nu}\frac{dx}{3dt_f}} = \frac{1}{1 + \frac{u_{sl}}{\tau_w}\frac{dx\,\rho_f}{3\,dt_f}} \tag{A3}$$

where u_{sl} is the slip velocity and $\dot{\gamma}_{f,w}$ the fluid shear rate at the boundary. Since the node is at the wall, τ_w equals the local shear stress

$$\tau_w = ((C_s \cdot dx)^2 \dot{\gamma}_{f,w} + \nu_f)\dot{\gamma}_{f,w} \tag{A4}$$

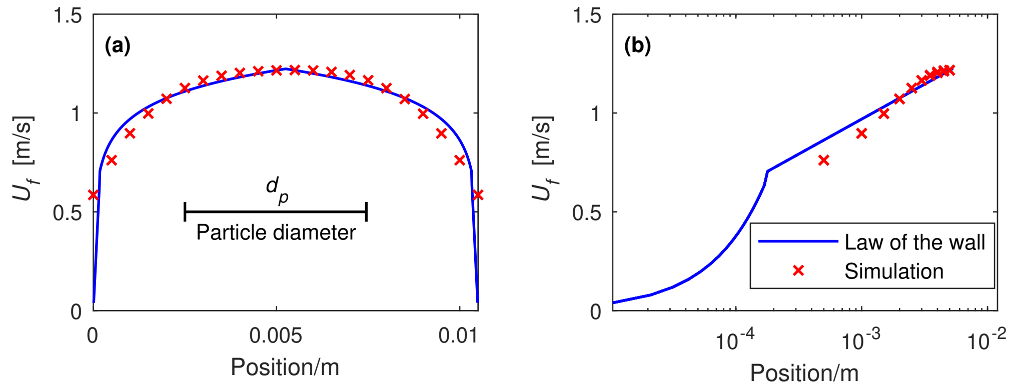

Figure A1. Turbulent pure fluid velocity across the channel: the law of the wall (solid blue line) compared with an LBM based large eddy simulation with the proposed Navier's slip boundary condition (red crosses), in (a) linear plot, and (b) semi-log plot. The inclined angle of the flume corresponds to a moderate Shields number $\tau* = 0.047$ in Figure 3. Note the channel is as wide as $\sim 2d_p$.

Assuming the second layer of nodes from the wall are right out of the viscous sublayer ($y^+ = 10.8$), then the dimensionless velocity there is 10.8. Extrapolating the logarithmic-law to the wall gives the slip velocity as

$$u_{sl} = 2.35u_\tau. \tag{A5}$$

Then Eqn (A1,A3,A4,A5) together give the analytical Navier's slip boundary condition for turbulent channel flow in LBM based LES.

Figure A1 shows the comparison between the law of the wall and an LBM based large eddy simulation with the proposed Navier's slip boundary condition. The simulated fluid velocity match the law of the wall very well. This simulation also serves as a tool to calibrate the value of $C_s = 0.27$ with the resolution of $dx = 0.005$m. The value of C_s and the grid spacing are used throughout this paper for the simulations in which the fluid is water. With the help of the proposed boundary condition, the shown LBM simulation whose resolutions dx is equivalent to $\sim 15\delta x_K$, is much faster than DNS without losing much accuracy on the fluid velocity.

Appendix B Validation of the DEM-LBM algorithm: single sphere settling, bouncing and rotation

As a validation of the DEM-LBM algorithm, single particle tests are performed to examine the linear and angular momentum exchanges between fluid and solid. When an immersed particle impacts a flat surface perpendicularly, the restitution coefficient is influenced by the Stokes number on collision $St_{im} = (1/9)(\rho_s d_p V_{im}/\eta)$, where V_{im} is the impact velocity (Gondret et al., 2002). Particularly, as shown by Ten Cate et al. (2002), when St_{im} is small, the sphere settles onto the surface gently without bouncing back. The bounce starts and the restitution coefficient increases as St_{im} increases above 10, and it approaches the dry value as St_{im} increases even further above 400 (X. Li et al., 2012). Herein we set up DEM-LBM simulations corresponding to the experiments in which $St_{im} = 0.19$ (a Nylon bearing in silicon oil) and $St_{im} = 65$ (a steel sphere in an aqueous glycerol solution), representing the settling and moderate bouncing regimes respectively. The sphere is initially stationary and then released to descend under gravity before impacting the bottom wall. The material properties are listed in Table B1.

Table B1. Material properties in the single sphere tests

		Settle	Bounce	Rotate
ρ_f	[kg·m^{-3}]	970	1203	1000
η	[Pa·s]	0.373	0.0502	0.833
ρ_s	[kg·m^{-3}]	1120	7780	2550
d_p	[mm]	15	9.5	5.2

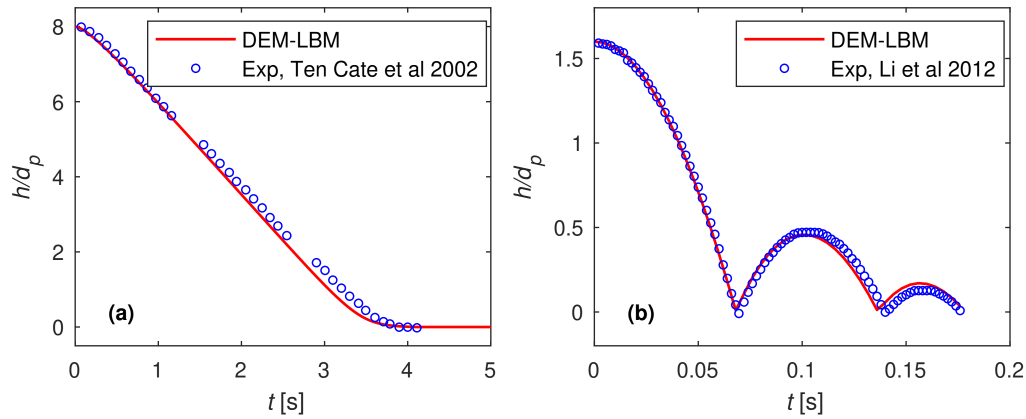

Figure B1. Results of the single sphere tests as Validation of DEM-LBM. Sphere normal trajectory comparisons with experiments for (a) settling and (b) bouncing.

In Figure B1 (a), the sphere is slightly denser than the surrounding viscous fluid and settles gently at the bottom. The match of the terminal velocity (slopes of the trajectories, within 5% relative error), which is reached long before landing, indicates that the linear momentum exchange between fluid and solid is correct. The velocity of the simulated sphere decreases slowly when it is approaching the bottom in agreement with the experiment, showing the hydrodynamic lubrication force is resolved correctly when solid boundaries are getting close. In Figure B1 (b), the sphere bounces multiple times and the simulation matches the first three collisions. Capturing the above two impact problems shows the DEM-LBM algorithm is capable of simulating the immersed particle interaction problems accurately, regardless of particle speed relative to the ambient fluid.

Besides the linear momentum exchange, we also need to examine how accurate the angular momentum is resolved because torque transfer can be evident due to the shear flow near the bed surface in sediment transport problems. Simulations in which an immersed single sphere is rotating at a fixed position are tested with the rotational velocity Ω varied by 1000 times. The fluid torque experienced by the sphere is compared with the analytical solution of the Stoke's flow solution $T = 8\pi\eta\Omega R_p^3$ as shown in Figure B2. The maximum relative error is smaller than 11% over the wide span of the tested rotational speeds. The slight error is mostly from the discrete representation of the spherical boundaries on the fluid lattice, which could be reduced further by refining the mesh.

Open Research

The data, DEM-LBM solver and the continuum models are available via the following link: `https://doi.org/10.6084/m9.figshare.16832560` (Q. Zhang et al., 2022).

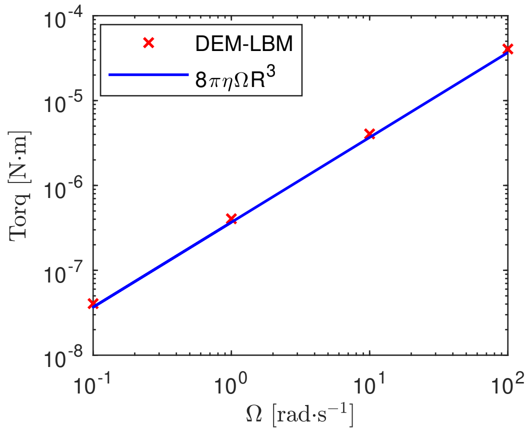

Figure B2. Fluid torque exerted on a rotating sphere over a large span of rotational velocity.

Acknowledgments

Research was sponsored by the Army Research Laboratory and was accomplished under Grant Number W911NF-16-1-0440. The views and conclusions contained in this document are those of the authors and should not be interpreted as representing the official policies, either expressed or implied, of the Army Research Laboratory or the U.S. Government. The U.S. Government is authorized to reproduce and distribute reprints for Government purposes notwithstanding any copyright notation herein. Q.Z. also thanks Patrick Mutabaruka for the help on implementing the DEM-LBM code and Guowei Zhang for the advice on parallel computing.

References

Aidun, C., & Clausen, J. (2010). Lattice-boltzmann method for complex flows. *Annual review of fluid mechanics*, *42*, 439–472.

Allen, B., & Kudrolli, A. (2017). Depth resolved granular transport driven by shearing fluid flow. *Physical Review Fluids*, *2*(2), 024304.

Allen, B., & Kudrolli, A. (2018). Granular bed consolidation, creep, and armoring under subcritical fluid flow. *Physical Review Fluids*, *3*(7), 074305.

Amarsid, L., Delenne, J., Mutabaruka, P., Monerie, Y., Perales, F., & Radjai, F. (2017). Viscoinertial regime of immersed granular flows. *Physical Review E*, *96*(1), 012901.

Ancey, C., & Pascal, I. (2020). Estimating mean bedload transport rates and their uncertainty. *Journal of Geophysical Research: Earth Surface*, *125*(7), e2020JF005534.

Ashida, K., & Michiue, M. (1973). Studies on bed-load transport rate in open channel flows. *IN: SEDIMENT TRANSPORTATION, VOLUME 1*.

Bagnold, R. (1980). An empirical correlation of bedload transport rates in flumes and natural rivers. In *Proceedings of the royal society of london a: Mathematical, physical and engineering sciences* (Vol. 372, pp. 453–473).

Banari, A., Mauzole, Y., Hara, T., Grilli, S. T., & Janßen, C. F. (2015). The simulation of turbulent particle-laden channel flow by the lattice boltzmann method. *International Journal for Numerical Methods in Fluids*, *79*(10), 491–513.

Bandara, S., & Soga, K. (2015). Coupling of soil deformation and pore fluid flow using material point method. *Computers and geotechnics*, *63*, 199–214.

Baumgarten, A., & Kamrin, K. (2019). A general fluid–sediment mixture model and constitutive theory validated in many flow regimes. *Journal of Fluid Mechan-*

ics, *861*, 721–764.

Beetstra, R., van der Hoef, M., & Kuipers, J. (2007). Drag force of intermediate reynolds number flow past mono-and bidisperse arrays of spheres. *AIChE journal*, *53*(2), 489–501.

Benavides, S. J., Deal, E., Rushlow, M., Venditti, J. G., Zhang, Q., Kamrin, K., & Perron, J. T. (2021). The impact of intermittency on bed load sediment transport. *Geophysical Research Letters*, e2021GL096088.

Berzi, D., & Fraccarollo, L. (2015). Turbulence locality and granularlike fluid shear viscosity in collisional suspensions. *Physical review letters*, *115*(19), 194501.

Bonnoit, C., Darnige, T., Clement, E., & Lindner, A. (2010). Inclined plane rheometry of a dense granular suspension. *Journal of Rheology*, *54*(1), 65–79.

Boutt, D. F., Cook, B. K., McPherson, B. J., & Williams, J. (2007). Direct simulation of fluid-solid mechanics in porous media using the discrete element and lattice-boltzmann methods. *Journal of Geophysical Research: Solid Earth*, *112*(B10).

Bouzidi, M., Firdaouss, M., & Lallemand, P. (2001). Momentum transfer of a boltzmann-lattice fluid with boundaries. *Physics of fluids*, *13*(11), 3452–3459.

Boyer, F., Guazzelli, É., & Pouliquen, O. (2011). Unifying suspension and granular rheology. *Physical Review Letters*, *107*(18), 188301.

Camenen, B. (2007). Simple and general formula for the settling velocity of particles. *Journal of Hydraulic Engineering*, *133*(2), 229–233.

Chauchat, J. (2018). A comprehensive two-phase flow model for unidirectional sheetflows. *Journal of Hydraulic Research*, *56*(1), 15–28.

Chauchat, J., Cheng, Z., Nagel, T., Bonamy, C., & Hsu, T.-J. (2017). Sedfoam-2.0: a 3-d two-phase flow numerical model for sediment transport. *Geoscientific Model Development*, *10*(12), 4367–4392.

Chauchat, J., & Guillou, S. (2008). On turbulence closures for two-phase sediment-laden flow models. *Journal of Geophysical Research: Oceans*, *113*(C11).

Chen, H., Chen, S., & Matthaeus, W. (1992). Recovery of the navier-stokes equations using a lattice-gas boltzmann method. *Physical review A*, *45*(8), R5339.

Chen, S., & Doolen, G. (1998). Lattice boltzmann method for fluid flows. *Annual review of fluid mechanics*, *30*(1), 329–364.

Cheng, N., Wei, M., Chiew, Y., Lu, Y., & Emadzadeh, A. (2020). Combined effects of mean flow and turbulence on sediment pickup rate. *Water Resources Research*, *56*(2), e2019WR026181.

Cosserat, E., & Cosserat, F. (1909). *Théorie des corps déformables.* A. Hermann et fils.

Da Cruz, F., Emam, S., Prochnow, M., Roux, J., & Chevoir, F. (2005). Rheophysics of dense granular materials: Discrete simulation of plane shear flows. *Physical Review E*, *72*(2), 021309.

Deal, E., Venditti, J., Benavides, S., Bradley, R., Zhang, Q., Kamrin, K., & Perron, J. T. (2021). Grain shape effects in bed load sediment transport. `https://eartharxiv.org/repository/view/2755/`.

Derksen, J. (2011). Simulations of granular bed erosion due to laminar shear flow near the critical shields number. *Physics of Fluids*, *23*(11), 113303.

Derksen, J. (2014). Simulations of hindered settling of flocculating spherical particles. *International journal of multiphase flow*, *58*, 127–138.

Derksen, J. (2015). Simulations of granular bed erosion due to a mildly turbulent shear flow. *Journal of Hydraulic Research*, *53*(5), 622–632.

Dey, S., & Ali, S. Z. (2017). Mechanics of sediment transport: Particle scale of entrainment to continuum scale of bedload flux. *Journal of Engineering Mechanics*, *143*(11), 04017127.

Di Felice, R. (1994). On the voidage function in two-phase multiparticle systems. *Int. J. Multiphase Flow*, *20*, 153–159.

Diplas, P., Dancey, C. L., Celik, A. O., Valyrakis, M., Greer, K., & Akar, T. (2008). The role of impulse on the initiation of particle movement under turbulent flow conditions. *Science*, *322*(5902), 717–720.

Elghannay, H. A., & Tafti, D. K. (2018). Sensitivity of numerical parameters on dem predictions of sediment transport. *Particulate Science and Technology*, *36*(4), 438–446.

Engelund, F., & Fredsøe, J. (1976). A sediment transport model for straight alluvial channels. *Hydrology Research*, *7*(5), 293–306.

Eshghinejadfard, A., Abdelsamie, A., Hosseini, S. A., & Thevenin, D. (2017). Immersed boundary lattice boltzmann simulation of turbulent channel flows in the presence of spherical particles. *International Journal of Multiphase Flow*, *96*, 161–172.

Feng, Z., & Michaelides, E. (2009). Robust treatment of no-slip boundary condition and velocity updating for the lattice-boltzmann simulation of particulate flows. *Computers & Fluids*, *38*(2), 370–381.

Ferdowsi, B., Ortiz, C. P., Houssais, M., & Jerolmack, D. J. (2017). River-bed armouring as a granular segregation phenomenon. *Nature communications*, *8*(1), 1–10.

Fernandez-Luque, R., & Van Beek, R. (1976). Erosion and transport of bed-load sediment. *Journal of hydraulic research*, *14*(2), 127–144.

Finn, J. R., Li, M., & Apte, S. V. (2016). Particle based modelling and simulation of natural sand dynamics in the wave bottom boundary layer. *Journal of Fluid Mechanics*, *796*, 340–385.

Gomez, B. (1991). Bedload transport. *Earth-Science Reviews*, *31*(2), 89–132.

Gondret, P., Lance, M., & Petit, L. (2002). Bouncing motion of spherical particles in fluids. *Physics of fluids*, *14*(2), 643–652.

Guan, L., Salinas, J., Zgheib, N., & Balachandar, S. (2021). The role of bed-penetrating kelvin–helmholtz vortices on local and instantaneous bedload sediment transport. *Journal of Fluid Mechanics*, *911*.

Guo, J. (2015). Sidewall and non-uniformity corrections for flume experiments. *Journal of Hydraulic Research*, *53*(2), 218–229.

Guo, Z., Zheng, C., & Shi, B. (2002). Discrete lattice effects on the forcing term in the lattice boltzmann method. *Physical review E*, *65*(4), 046308.

Heyman, J., Bohorquez, P., & Ancey, C. (2016). Entrainment, motion, and deposition of coarse particles transported by water over a sloping mobile bed. *Journal of Geophysical Research: Earth Surface*, *121*(10), 1931–1952.

Hill, K., & Tan, D. (2017). Granular flows applied to gravel-bed rivers: particle-scale studies of the mobilization of a gravel bed by the addition of fines. *Gravel-Bed Rivers: Processes and Disasters*, 73–95.

Holloway, W., Sun, J., & Sundaresan, S. (2012). Effect of microstructural anisotropy on the fluid–particle drag force and the stability of the uniformly fluidized state. *Journal of Fluid Mechanics*, *713*, 27–49.

Hou, S., Sterling, J., Chen, S., & Doolen, G. (1994). A lattice boltzmann subgrid model for high reynolds number flows. *arXiv preprint comp-gas/9401004*.

Houssais, M., Ortiz, C. P., Durian, D. J., & Jerolmack, D. J. (2015). Onset of sediment transport is a continuous transition driven by fluid shear and granular creep. *Nature communications*, *6*(1), 1–8.

Jop, P., Forterre, Y., & Pouliquen, O. (2006). A constitutive law for dense granular flows. *Nature*, *441*(7094), 727–730.

Kamrin, K. (2019). Non-locality in granular flow: Phenomenology and modeling approaches. *Frontiers in Physics*, *7*, 116.

Kamrin, K., & Henann, D. (2015). Nonlocal modeling of granular flows down inclines. *Soft matter*, *11*(1), 179–185.

Kamrin, K., & Koval, G. (2012). Nonlocal constitutive relation for steady granular flow. *Physical Review Letters*, *108*(17), 178301.

Kamrin, K., & Koval, G. (2014). Effect of particle surface friction on nonlocal constitutive behavior of flowing granular media. *Computational Particle Mechanics*, *1*(2), 169–176.

Kim, S., & Kamrin, K. (2020). Power-law scaling in granular rheology across flow geometries. *Physical Review Letters*, *125*(8), 088002.

Kloss, C., Goniva, C., Hager, A., Amberger, S., & Pirker, S. (2012). Models, algorithms and validation for opensource dem and cfd–dem. *Progress in Computational Fluid Dynamics, an International Journal*, *12*(2-3), 140–152.

Kock, I., & Huhn, K. (2007). Influence of particle shape on the frictional strength of sediments—a numerical case study. *Sedimentary Geology*, *196*(1-4), 217–233.

Komatsu, T. S., Inagaki, S., Nakagawa, N., & Nasuno, S. (2001). Creep motion in a granular pile exhibiting steady surface flow. *Physical review letters*, *86*(9), 1757.

Kriebitzsch, S., Van der Hoef, M., & Kuipers, J. (2013). Fully resolved simulation of a gas-fluidized bed: a critical test of dem models. *Chemical Engineering Science*, *91*, 1–4.

Ladd, A. (1994). Numerical simulations of particulate suspensions via a discretized boltzmann equation. part 1. theoretical foundation. *Journal of fluid mechanics*, *271*, 285–309.

Lajeunesse, E., Malverti, L., & Charru, F. (2010). Bed load transport in turbulent flow at the grain scale: Experiments and modeling. *Journal of Geophysical Research: Earth Surface*, *115*(F4).

Li, L., & Sawamoto, M. (1995). Multi-phase model on sediment transport in sheet-flow regime under oscillatory flow. *Coastal Engineering in Japan*, *38*(2), 157–178.

Li, X., Hunt, M., & Colonius, T. (2012). A contact model for normal immersed collisions between a particle and a wall. *Journal of fluid mechanics*, *691*, 123–145.

Liu, C., Shan, Y., & Nepf, H. (2021). Impact of stem size on turbulence and sediment resuspension under unidirectional flow. *Water Resources Research*, *57*(3), e2020WR028620.

Liu, D., & Henann, D. L. (2017). Non-local continuum modelling of steady, dense granular heap flows. *Journal of Fluid Mechanics*, *831*, 212–227.

Ma, T., Yu, Y., Chen, X., & Zhou, Q. (2020). Effect of anisotropic microstructures on fluid–particle drag in low-reynolds-number monodisperse gas–solid suspensions. *AIChE Journal*, *66*(4), e16910.

MacKenzie, L. G., & Eaton, B. C. (2017). Large grains matter: contrasting bed stability and morphodynamics during two nearly identical experiments. *Earth Surface Processes and Landforms*, *42*(8), 1287–1295.

MacKenzie, L. G., Eaton, B. C., & Church, M. (2018). Breaking from the average: Why large grains matter in gravel-bed streams. *Earth Surface Processes and Landforms*, *43*(15), 3190–3196.

Maurin, R., Chauchat, J., Chareyre, B., & Frey, P. (2015). A minimal coupled fluid-discrete element model for bedload transport. *Physics of Fluids*, *27*(11), 113302.

Maurin, R., Chauchat, J., & Frey, P. (2016). Dense granular flow rheology in turbulent bedload transport. *Journal of Fluid Mechanics*, *804*, 490–512.

Maurin, R., Chauchat, J., & Frey, P. (2018). Revisiting slope influence in turbulent bedload transport: consequences for vertical flow structure and transport rate scaling. *Journal of Fluid Mechanics*, *839*, 135–156.

Mei, R., Yu, D., Shyy, W., & Luo, L. (2002). Force evaluation in the lattice boltzmann method involving curved geometry. *Physical Review E*, *65*(4), 041203.

Meyer-Peter, E., & Müller, R. (1948). Formulas for bed-load transport. In *Iahsr 2nd meeting, stockholm, appendix 2.*

Mueth, D. M. (2003). Measurements of particle dynamics in slow, dense granular couette flow. *Physical Review E*, *67*(1), 011304.

Mutabaruka, P., Delenne, J.-Y., Soga, K., & Radjai, F. (2014). Initiation of immersed granular avalanches. *Physical Review E*, *89*(5), 052203.
Mutabaruka, P., & Kamrin, K. (2018). Simulation technique for slurries interacting with moving parts and deformable solids with applications. *Computational Particle Mechanics*, *5*(2), 239–267.
Ni, W., & Capart, H. (2018). Stresses and drag in turbulent bed load from refractive index-matched experiments. *Geophysical Research Letters*, *45*(14), 7000–7009.
Niño, Y., García, M., & Ayala, L. (1994). Gravel saltation: 1. experiments. *Water resources research*, *30*(6), 1907–1914.
Ojha, S. P., Mazumder, B., Carstensen, S., & Fredsoe, J. (2019). Externally generated turbulence by a vertically oscillating grid plate and its impact on sediment transport rate. *Coastal Engineering Journal*, *61*(4), 444–459.
Pähtz, T., Clark, A. H., Valyrakis, M., & Durán, O. (2020). The physics of sediment transport initiation, cessation, and entrainment across aeolian and fluvial environments. *Reviews of Geophysics*, *58*(1), e2019RG000679.
Pähtz, T., & Durán, O. (2018a). The cessation threshold of nonsuspended sediment transport across aeolian and fluvial environments. *Journal of Geophysical Research: Earth Surface*, *123*(8), 1638–1666.
Pähtz, T., & Durán, O. (2018b). Universal friction law at granular solid-gas transition explains scaling of sediment transport load with excess fluid shear stress. *Physical Review Fluids*, *3*(10), 104302.
Pähtz, T., & Durán, O. (2020). Unification of aeolian and fluvial sediment transport rate from granular physics. *Physical Review Letters*, *124*(16), 168001.
Pähtz, T., Liu, Y., Xia, Y., Hu, P., He, Z., & Tholen, K. (2021). Unified model of sediment transport threshold and rate across weak and intense subaqueous bedload, windblown sand, and windblown snow. *Journal of Geophysical Research: Earth Surface*, *126*(4), e2020JF005859.
Pailha, M., & Pouliquen, O. (2009). A two-phase flow description of the initiation of underwater granular avalanches. *Journal of Fluid Mechanics*, *633*, 115.
Parker, G. (1978). Self-formed straight rivers with equilibrium banks and mobile bed. part 2. the gravel river. *Journal of Fluid mechanics*, *89*(1), 127–146.
Plimpton, S. (1995). Fast parallel algorithms for short-range molecular dynamics. *Journal of computational physics*, *117*(1), 1–19.
Reid, I., & Laronne, J. B. (1995). Bed load sediment transport in an ephemeral stream and a comparison with seasonal and perennial counterparts. *Water Resources Research*, *31*(3), 773–781.
Revil-Baudard, T., Chauchat, J., Hurther, D., & Barraud, P. (2015). Investigation of sheet-flow processes based on novel acoustic high-resolution velocity and concentration measurements. *Journal of Fluid Mechanics*, *767*, 1–30.
Richardson, J., & Zaki, W. (1954). Sedimentation and fluidisation: Part i. *Trans. Instn Chem. Engrs*, *32*, 35–53.
Rouse, H. (1937). Modern conceptions of the mechnics of turbulence. *Transactions American Soc. of Civil Engineers*, *102*, 463–505.
Rousseau, G., & Ancey, C. (n.d.). An experimental investigation of turbulent free-surface flows over a steep permeable bed.
Schiller, L. (1933). Über die grundlegenden berechnungen bei der schwerkraftaufbereitung. *Z. Vereines Deutscher Inge.*, *77*, 318–321.
Schmeeckle, M. (2014). Numerical simulation of turbulence and sediment transport of medium sand. *Journal of Geophysical Research: Earth Surface*, *119*(6), 1240–1262.
Schmeeckle, M. (2015). The role of velocity, pressure, and bed stress fluctuations in bed load transport over bed forms: numerical simulation downstream of a backward-facing step. *Earth Surface Dynamics*, *3*(1), 105.
Schmeeckle, M., & Nelson, J. (2003). Direct numerical simulation of bedload transport using a local, dynamic boundary condition. *Sedimentology*, *50*(2), 279–

301.
Sekine, M., & Kikkawa, H. (1992). Mechanics of saltating grains. ii. *Journal of Hydraulic Engineering*, *118*(4), 536–558.
Shields, I. (1936). Anwendung der ahnlichkeitmechanik und der turbulenzforschung auf die gescheibebewegung, mitt. preuss ver. *Anst., Berlin*, *26*.
Siavoshi, S., Orpe, A. V., & Kudrolli, A. (2006). Friction of a slider on a granular layer: Nonmonotonic thickness dependence and effect of boundary conditions. *Physical Review E*, *73*(1), 010301.
Silbert, L., Landry, J., & Grest, G. (2003). Granular flow down a rough inclined plane: transition between thin and thick piles. *Physics of Fluids*, *15*(1), 1–10.
Simonin, O. (1989). Numerical study on phase dispersion mechanisms in turbulent bubbly flows. In *Int. conf. on mechanics of two-phase flows* (pp. 163–165).
Smagorinsky, J. (1963). General circulation experiments with the primitive equations: I. the basic experiment. *Monthly weather review*, *91*(3), 99–164.
Succi, S. (2001). *The lattice boltzmann equation: for fluid dynamics and beyond.* Oxford university press.
Sumer, B. M., Chua, L. H., Cheng, N.-S., & Fredsøe, J. (2003). Influence of turbulence on bed load sediment transport. *Journal of Hydraulic Engineering*, *129*(8), 585–596.
Swope, W., Andersen, H., Berens, P., & Wilson, K. (1982). A computer simulation method for the calculation of equilibrium constants for the formation of physical clusters of molecules: Application to small water clusters. *The Journal of chemical physics*, *76*(1), 637–649.
Ten Cate, A., Nieuwstad, C., Derksen, J., & Van den Akker, H. (2002). Particle imaging velocimetry experiments and lattice-boltzmann simulations on a single sphere settling under gravity. *Physics of Fluids*, *14*(11), 4012–4025.
Trulsson, M., Andreotti, B., & Claudin, P. (2012). Transition from the viscous to inertial regime in dense suspensions. *Physical review letters*, *109*(11), 118305.
Uth, M., Crüger, A., & Herwig, H. (2013). A new partial slip boundary condition for the lattice-boltzmann method. In *International conference on nanochannels, microchannels, and minichannels* (Vol. 55591, p. V001T12A001).
Vargas-Luna, A., Crosato, A., & Uijttewaal, W. S. (2015). Effects of vegetation on flow and sediment transport: comparative analyses and validation of predicting models. *Earth Surface Processes and Landforms*, *40*(2), 157–176.
Venditti, J. (2013). 9.10 bedforms in sand-bedded rivers. In J. F. Shroder (Ed.), *Treatise on geomorphology* (p. 137-162). San Diego: Academic Press. Retrieved from `https://www.sciencedirect.com/science/article/pii/B9780123747396002359` doi: https://doi.org/10.1016/B978-0-12-374739-6.00235-9
Venditti, J., Nelson, P. A., Bradley, R. W., Haught, D., & Gitto, A. B. (2017). Bedforms, structures, patches, and sediment supply in gravel-bed rivers. *Gravel-Bed Rivers: Processes and Disasters, edited by: Tsutsumi, D. and Laronne, JB, John Wiley & Sons, Chichester, England*, 439–466.
Walton, O. (1994). Effects of interparticle friction and particle shape on dynamic angles of repose via particle-dynamics simulation. In *Proc. conf. mechanics and statistical physics of particulate materials, june* (pp. 8–10).
Wang, K., Chai, Z., Hou, G., Chen, W., & Xu, S. (2018). Slip boundary condition for lattice boltzmann modeling of liquid flows. *Computers & Fluids*, *161*, 60–73.
Wang, L., Peng, C., Guo, Z., & Yu, Z. (2016). Lattice boltzmann simulation of particle-laden turbulent channel flow. *Computers & Fluids*, *124*, 226–236.
Wiacek, J., Molenda, M., Horabik, J., & Ooi, J. Y. (2012). Influence of grain shape and intergranular friction on material behavior in uniaxial compression: Experimental and dem modeling. *Powder Technology*, *217*, 435–442.

Wiberg, P., & Smith, D. (1989). Model for calculating bed load transport of sediment. *Journal of hydraulic engineering*, *115*(1), 101–123.
Wong, M. (2003). Does the bedload equation of meyer-peter and müller fit its own data. In *Proceedings, 30th congress, international association of hydraulic research, thessaloniki, jfk competition* (Vol. 73, p. 80).
Wong, M., & Parker, G. (2006). Reanalysis and correction of bed-load relation of meyer-peter and müller using their own database. *Journal of Hydraulic Engineering*, *132*(11), 1159–1168.
Wylie, J., Koch, D., & Ladd, A. (2003). Rheology of suspensions with high particle inertia and moderate fluid inertia. *Journal of Fluid Mechanics*, *480*, 95.
Yager, E., Kirchner, J., & Dietrich, W. (2007). Calculating bed load transport in steep boulder bed channels. *Water Resources Research*, *43*(7).
Yalin, M., & da Silva, A. F. (2001). Fluvial processes. iahr monograph. *International Association for Hydraulic Research, Delft*.
Yoshizawa, A. (1993). Subgrid-scale modeling suggested by a two-scale dia. In *Computational wind engineering 1* (pp. 69–76). Elsevier.
Yu, H., Girimaji, S., & Luo, L. (2005). Dns and les of decaying isotropic turbulence with and without frame rotation using lattice boltzmann method. *Journal of Computational Physics*, *209*(2), 599–616.
Zhang, C., Soga, K., Kumar, K., Sun, Q., & Jin, F. (2017). Numerical study of a sphere descending along an inclined slope in a liquid. *Granular Matter*, *19*(4), 1–19.
Zhang, Q., Deal, E., Perron, J. T., Venditti, J. G., Benavides, S. J., Rushlow, M., & Kamrin, K. (2022). *Data for "fluid-driven transport of round sediment particles: from discrete simulations to continuum modeling".* Retrieved from `https://figshare.com/articles/dataset/Fluid-driven_transport_of_round_sediment_particles_from_discrete_simulations_to_continuum_modeling/16832560` doi: 10.6084/m9.figshare.16832560.v8
Zhang, Q., & Kamrin, K. (2017). Microscopic description of the granular fluidity field in nonlocal flow modeling. *Physical review letters*, *118*(5), 058001.